

# Shedding Light on Low Surface Brightness Galaxies in Dark Energy Survey with Transformers

H. Thuruthipilly<sup>1</sup>, Junais<sup>1</sup>, A. Pollo<sup>1,2</sup>, U. Sureshkumar<sup>2,3</sup>, M. Grespan<sup>1</sup>, P. Sawant<sup>1</sup>, K. Małek<sup>1</sup>, and A. Zdrozny<sup>1</sup>

<sup>1</sup> National Centre for Nuclear Research, Warsaw, Poland

e-mail: Hareesh.Thuruthipilly@ncbj.gov.pl,

e-mail: Junais@ncbj.gov.pl, e-mail: Agnieszka.Pollo@ncbj.gov.pl

<sup>2</sup> Jagiellonian University, Kraków, Poland

<sup>3</sup> Wits Centre for Astrophysics, School of Physics, University of the Witwatersrand, Johannesburg, South Africa.

Received XXX / Accepted YYY

## ABSTRACT

**Context.** Low surface brightness galaxies (LSBGs) which are defined as galaxies that are fainter than the night sky, play a crucial role in understanding galaxy evolution and cosmological models. Upcoming large-scale surveys like Rubin Observatory Legacy Survey of Space and Time (LSST) and Euclid are expected to observe billions of astronomical objects. In this context, using semi-automatic methods to identify LSBGs would be a highly challenging and time-consuming process and demand automated or machine learning-based methods to overcome this challenge.

**Aims.** We study the use of transformer models in separating LSBGs from artefacts in the data from the Dark Energy Survey (DES) data release 1. Using the transformer models, we then search for new LSBGs from the DES that the previous searches may have missed. Properties of the newly found LSBGs are investigated, along with an analysis of the properties of the total LSBG sample in DES.

**Methods.** We created eight different transformer models and used an ensemble of these eight models to identify LSBGs. This was followed by a single-component Sérsic model fit and a final visual inspection to filter out false positives.

**Results.** Transformer models achieved an accuracy  $\sim 94\%$  in separating the LSBGs from artefacts. In addition, we identified 4083 new LSBGs in DES, adding an additional  $\sim 17\%$  to the LSBGs already known in DES. This also increased the number density of LSBGs in DES to  $5.5 \text{ deg}^{-2}$ . The new LSBG sample consists of mainly blue and compact galaxies. We performed a clustering analysis of the LSBGs in DES using an angular two-point auto-correlation function and found that LSBGs cluster more strongly than their high surface brightness counterparts. This effect is driven by the red LSBG. We associated 1310 LSBGs with galaxy clusters and identified 317 among them as ultra-diffuse galaxies (UDGs). We found that these cluster LSBGs are getting bluer and larger in size towards the edge of the clusters when compared with those in the centre.

**Conclusions.** Transformer models have the potential to be on par with convolutional neural networks as state-of-the-art algorithms in analysing astronomical data. The significant number of LSBGs identified from the same dataset using a different algorithm highlights the substantial impact of the methodology on finding LSBGs. The reported number density of LSBGs is only a lower estimate and can be expected to increase with the advent of surveys with better image quality and more advanced methodologies.

**Key words.** Low Surface Brightness Galaxies; Galaxy Surveys; Machine Learning

## 1. Introduction

Low-surface-brightness galaxies (LSBGs) are most often defined as galaxies with a central surface brightness fainter than the night sky or galaxies with  $B$ -band central surface brightness  $\mu_0(B)$  below a certain threshold value. In literature, the threshold values of  $\mu_0(B)$  for classifying a galaxy as LSBG vary among different works, ranging from  $\mu_0(B) \geq 23.0 \text{ mag arcsec}^{-2}$  (Bothun et al. 1997) to  $\mu_0(B) \geq 22.0 \text{ mag arcsec}^{-2}$  (Burkholder et al. 2001).

It is estimated that the LSBGs only contribute a few percentages ( $< 10\%$ ) to the local luminosity and stellar mass density of the observable universe (Bernstein et al. 1995; Driver 1999; Hayward et al. 2005; Martin et al. 2019). However, LSBGs are considered to account for a significant fraction ( $30\% \sim 60\%$ ) of the total number density of galaxies (McGaugh 1996; Bothun et al. 1997; O’Neil & Bothun 2000; Habertzettl et al. 2007; Martin et al. 2019), and as much as 15% of the dynamical mass content of the universe (Driver 1999; Minchin et al. 2004). These

numbers imply that LSBGs can contribute significantly to our understanding of the physics of galaxy evolution and cosmological models. However, as their name indicates, LSBGs are very faint systems, and due to the observational challenges in detecting them, LSBGs remain mostly an unexplored realm.

In recent years, despite the observational challenges, advances in digital imaging have improved our ability to detect LSBGs. The first known and the largest LSBG to be identified and verified is Malin 1, serendipitously discovered by Bothun et al. (1987) during a survey of galaxies of low surface brightness in the Virgo cluster. Notably, Malin 1 is the largest spiral galaxy known until today (e.g., Impey et al. 1988; Junais et al. 2020; Galaz et al. 2022). Current searches for LSBGs have shown that they exhibit a wide range of physical sizes (E Greene et al. 2022) and can be found in various types of environments, ranging from satellites of local nearby galaxies (Danieli et al. 2017; Cohen et al. 2018), ultra-faint satellites of the Milky Way (McConnachie 2012; Simon 2019), galaxies found in the field (Leisman et al. 2017; Prole et al. 2021), to members of massive

galaxy clusters like Virgo (Mihos et al. 2015, 2017; Junais et al. 2022) and Coma (van Dokkum et al. 2015; Koda et al. 2015).

LSBGs also consist of several sub-classes based on their physical size, surface brightness and gas content. Ultra-diffuse galaxies (UDGs) represent a subclass of LSBGs characterized by their considerable size, comparable to that of Milky Way-like galaxies, yet exhibiting very faint luminosities akin to dwarf galaxies. Although the term ‘UDG’ was coined by van Dokkum et al. (2015), such galaxies were identified in several earlier studies in the literature (Sandage & Binggeli 1984; McGaugh & Bothun 1994; Dalcanton et al. 1997; Conselice et al. 2003a). Similarly, giant LSBGs (GLSBGs) form another sub-class of LSBGs that are extremely gas-rich ( $M_{\text{HI}} > 10^{10} M_{\odot}$ ), faint and extended (Sprayberry et al. 1995; Saburova et al. 2023). The formation and evolution of extreme classes like UDGs and GLSBGs are still debated (Amorisco & Loeb 2016; Di Cintio et al. 2017; Saburova et al. 2021; Benavides et al. 2023; Laudato & Salzano 2023).

To comprehend the formation of various types LSBGs in different environments, studying them extensively across different environments (galaxy clusters vs field) over a large area of the sky is crucial. Recently, Greco et al. (2018) detected 781 LSBGs in the Hyper Suprime-Cam Subaru Strategic Program (HSC SSP) in a blind search covering around 200 deg<sup>2</sup> of the sky from the Wide layer of the HSC SSP. Similarly, in a recent study, Tanoglidis et al. (2021b) utilised a support vector machine (SVM) and visual inspection to analyse the first three years of data from the Dark Energy Survey (DES). They identified more than 20 000 LSBGs, which is currently the largest LSBG catalogue available.

A common feature observed in both of these untargeted searches for LSBGs was the significant presence of low-surface brightness artefacts. As pointed out in Tanoglidis et al. (2021b), these artefacts predominantly consist of diffuse light from nearby bright objects, galactic cirrus, star-forming tails of spiral arms and tidal streams. These artefacts typically pass the simple selection cuts based on photometric measurements and often make up the majority of the LSBG candidate sample. These contaminants need to be removed, which is often accomplished using semi-automated methods with a low success rate and visual inspection, which is more precise but time-consuming.

For example, in HSC SSP, Greco et al. (2018) applied selection cuts on the photometric measurements from SourceExtractor (Bertin & Arnouts 1996). This led to the selection of 20 838 LSBG candidates. Using a galaxy modelling pipeline based on `imfit` (Erwin 2015), the sample size was subsequently reduced to 1 521. However, after the visual inspection, only 781 candidates were considered confident LSBGs, which is around 4% of the preliminary candidate sample and 50% of the sample selected by the pipeline. Similarly, in DES, Tanoglidis et al. (2021b) shortlisted 419 895 LSBG candidates using the selection cuts on SourceExtractor photometric measurements. After applying a feature-based machine learning (ML) classification (SVM) on the photometric measurements, the candidate sample was further reduced to 44 979 objects. However, a significant number of false positives still remained, and only 23 790 were later classified as confident LSBGs. Therefore, these numbers indicate that the occurrence of LSBGs in these methods is roughly 5% for the initial selection and 50% for the subsequent selection.

The upcoming large-scale surveys, such as Legacy Survey of Space and Time (LSST; Ivezić et al. 2019) and Euclid (Euclid Collaboration et al. 2022), are expected to observe billions of astronomical objects. In this scenario, relying solely on photo-

metric selection cuts or semi-automated methods such as galaxy model fitting would not be practical to identify LSBGs confidently. Furthermore, the accuracy of the classification methodology between LSBGs and artefacts must be improved to achieve meaningful results. Hence, this situation demands more effective and efficient automation methodologies for the searches of LSBGs.

Recently, the advancements in deep learning have opened up a plethora of opportunities and have been widely applied in astronomy. Particularly for analysing astronomical images, convolutional neural networks (CNNs) have emerged as a state-of-the-art technique. For example, the CNNs have been used for galaxy classification (Pérez-Carrasco et al. 2019), galaxy merger identification (Pearson et al. 2022), supernova classification (Cabrera-Vives et al. 2017) and finding strong gravitational lenses (Schaefer et al. 2018; Davies et al. 2019; Rojas et al. 2022). One of the fascinating features of CNNs is their ability to directly process the image as input and learn the image features, making them one of the most popular and robust architectures in use today. Generally, the learning capacity of a neural network increases with the number of layers in the network. The first layers of the network learn the low-level features, and the last layers learn more complex features (Russakovsky et al. 2015; Simonyan & Zisserman 2015).

One of the main requirements for creating a trained CNN is a sufficiently large training dataset that can generalise the features of the data we are trying to analyse. Recently, Tanoglidis et al. (2021a) utilised a catalogue of over 20 000 LSBGs from DES to classify LSBGs from artefacts using a CNN for the first time and achieved an accuracy of 92% and a true positive rate of 94%.

While CNNs have been the dominant choice for analysing image data in astronomy, the current state-of-the-art models for computer vision are transformers. Transformers were initially introduced in natural language processing (NLP) as an attention-based model (Vaswani et al. 2017). The fundamental concept behind the transformer architecture is the attention mechanism, which has also found a broad range of applications in machine learning (Zhang et al. 2018; Fu et al. 2019; Parmar et al. 2019; Zhao et al. 2020; Tan et al. 2021). In the case of NLP, attention calculates the correlation of different positions of a single sequence to calculate a representation of the sequence. Later the idea was adapted to computer vision and has been used to produce state-of-the-art models for various image processing tasks like image classification (Wortsman et al. 2022), and image segmentation (Chen et al. 2023).

Generally, two categories of transformers are present in the literature. The first type integrates both CNNs and attention to perform the analysis. An example of this type is the Detection Transformer (DETR) proposed for end-to-end object detection by Carion et al. (2020). The key idea behind using CNNs and Transformers together is to leverage the strengths of both architectures. CNNs excel at local feature extraction, capturing low-level details, and spatial hierarchies, while attention layers excel at modelling global context and long-range dependencies. The second class of transformers is the models that do not use a CNN and operate entirely based on self-attention mechanisms. An example of this type is the Vision transformer (ViT) proposed for object classification by Dosovitskiy et al. (2021). ViTs have demonstrated remarkable performance in image classification tasks and have surpassed the accuracy of CNN-based models on various benchmark datasets (Dosovitskiy et al. 2021; Yu et al. 2022; Wortsman et al. 2022).

Even though transformers have been introduced very recently in astronomy, they have already found a wide variety

of applications. For example, the transformer models have been used to detect and analyse strong gravitational lensing systems (Thuruthipilly et al. 2022b,a; Huang et al. 2022; Jia et al. 2023), representing light curves which can be used further for classification or regression (Allam & McEwen 2021), and classifying multi-band light curves of different supernovae (SN) types (Pimentel et al. 2023).

In this paper, we explore the possibilities of transformers in classifying LSBGs from artefacts in DES and compare the performance of transformers with the CNNs presented in Tanoglidis et al. (2021a). We also use the transformer models to look for new LSBGs that the previous searches may have missed. For comparison purposes, throughout this work, we follow the LSBG definition from Tanoglidis et al. (2021b), based on the  $g$ -band mean surface brightness ( $\bar{\mu}_{eff}$ ) and the half-light radii ( $r_{1/2}$ ). We consider LSBGs as galaxies with  $\bar{\mu}_{eff} > 24.2$  mag arcsec<sup>-2</sup> and  $r_{1/2} > 2.5''$ .

The paper is organised as follows. Sect. 2 discusses the data we used to train our models and look for new LSBGs. Sect. 3 provides a brief overview of the methodology used in our study, including the models' architecture, information on how the models were trained, and the details about the visual inspection. The results of our analysis are presented in Sect. 4. A detailed discussion of our results and the properties of the newly identified LSBGs are analysed in Sect. 5 and Sect. 6 respectively. Further analysis of the clustering of LSBGs is presented in Sect. 7 and a detailed discussion on the UDGs, which are identified as a subsample of LSBGs, is presented in Sect. 8. Sect. 9 concludes our analysis by highlighting the significance of LSBGs, the impact of methodology in finding LSBGs, and the future prospect with LSST.

## 2. Data

### 2.1. Dark Energy Survey

The Dark Energy Survey (DES; Abbott et al. 2018, 2021) is a six-year observing program (2013-2019) covering  $\sim 5000$  deg<sup>2</sup> of the southern Galactic cap in the optical and near-infrared regime using the Dark Energy Camera (DECam) on the 4-m Blanco Telescope at the Cerro Tololo Inter-American Observatory (CTIO). The DECam focal plane comprises 62 2k  $\times$  4k charge-coupled devices (CCDs) dedicated to science imaging and 12 2k  $\times$  2k CCDs for guiding, focus, and alignment. The DECam field-of-view covers 3 deg<sup>2</sup> with a central pixel scale of 0.263 arcsec pixel<sup>-1</sup> (Flaugher et al. 2015). To address the gaps between CCDs, DES utilises a dithered exposure pattern (Neilsen et al. 2019) and combines the resulting individual exposures to form coadded images, which have dimensions of 0.73  $\times$  0.73 degrees (Morganson et al. 2018). The DES has observed the sky in *grizY* photometric bands with approximately 10 overlapping dithered exposures in each filter (90 sec in *griz*-bands and 45 sec in *Y*-band).

### 2.2. DES DR1 and the gold catalogue

In this work, we use the image data from the dark energy survey data release 1 (DES DR1; Abbott et al. 2018) and the DES Y3 gold coadd object catalogue (DES Y3\_gold\_2\_2.1) obtained from the first three years of the DES observations (Sevilla-Noarbe et al. 2021). The DES DR1 comprises optical and near-infrared imaging captured over 345 different nights between August 2013 and February 2016. The median  $3\sigma$  surface brightness limits of the  $g$ ,  $r$ , and  $i$ -bands of DES DR1 are 28.26, 27.86, and

27.37 mag arcsec<sup>-2</sup>, respectively (Tanoglidis et al. 2021b). It is worth mentioning that the DES source detection pipeline has not been optimised for detecting large, low surface-brightness objects (Morganson et al. 2018). Thus, the above-mentioned surface brightness values can be considered as the limits for detecting faint objects in each band. The gold catalogue shares the same single image processing, image coaddition, and object detection as the DES DR1. The objects in the gold catalogue were detected using SourceExtractor (Bertin & Arnouts 1996) and have undergone selection cuts on minimal image depth and quality, additional calibration, and deblending. The median coadd magnitude limit of the DES Y3 gold object catalogue at a signal-to-noise ratio (S/N) = 10 is  $g = 24.3$  mag,  $r = 24.0$  mag, and  $i = 23.3$  mag (Sevilla-Noarbe et al. 2021). The gold catalogue contains around 319 million astronomical objects, which we used for searching LSBGs in DES. For a detailed review and discussion on the data from the DES, please refer to Abbott et al. (2018) and Sevilla-Noarbe et al. (2021).

We reduced the number of objects processed in our study using preselections similar to Greco et al. (2018) and Tanoglidis et al. (2021b). We first removed objects classified as point-like objects in the gold catalogue, based on the  $i$ -band SourceExtractor SPREAD\_MODEL parameter and EXTENDED\_CLASS\_COADD as described in Tanoglidis et al. (2021b). In addition, we constrained the  $g$ -band half-light radius (FLUX\_RADIUS\_G) and surface brightness (MUE\_MEAN\_MODEL\_G) within the range of  $2.5'' < r_{1/2} < 20''$  and  $24.2 < \bar{\mu}_{eff} < 28.8$  mag arcsec<sup>-2</sup>, respectively. Furthermore, we also limited our sample to objects with colors (using the MAG\_AUTO magnitudes) in the range:

$$-0.1 < g - i < 1.4, \quad (1)$$

$$(g - r) > 0.7 \times (g - i) - 0.4, \quad (2)$$

$$(g - r) < 0.7 \times (g - i) + 0.4. \quad (3)$$

These color cuts are based on Greco et al. (2018) and Tanoglidis et al. (2021b). As mentioned by Greco et al. (2018), these color requirements will remove the spurious detections due to optical artefacts detected in all bands and blends of high-redshift galaxies. Finally, we also restricted the axis ratio (B\_IMAGE/A\_IMAGE) of each object to be greater than 0.3 to remove the artefacts like the highly elliptical diffraction spikes. Our complete selection criteria were based on the selection criteria presented in Appendix B of Tanoglidis et al. (2021b). After the preliminary selections using the SourceExtractor parameters from the DES Y3 gold catalogue, our sample contains 419 784 objects.

### 2.3. Training data

All of the trained, validated, and tested models in this study used the labelled dataset of LSBGs and artefacts identified from DES by Tanoglidis et al. (2021b). Below, we briefly summarise the primary steps taken by Tanoglidis et al. (2021b) in constructing the LSBG catalogue.

- (i) The SourceExtractor parameters from the DES Y3 gold coadd object catalogue presented by Sevilla-Noarbe et al. (2021) were used to create the initial selection cuts, as discussed in Sect. 2.2.
- (ii) The candidate sample was further reduced using an SVM to classify artefacts and LSBGs. The SVM was trained with a manually labelled set of  $\sim 8000$  objects (640 LSBGs) and using the SourceExtractor parameters as features for learning.

- (iii) From the candidate sample generated through SVM, over 20 000 artefacts were excluded upon visual inspection. Most of the rejected objects that had passed SVM's feature-based selection were found to be astronomical artefacts (such as galactic cirrus, star-forming extensions of spiral arms, and tidal streams) rather than instrumental artefacts (such as scattered light emitted by nearby bright objects) during visual inspection.
- (iv) Objects that passed the visual inspection were subjected to Sérsic model fitting and Galactic extinction correction. Following this, new selection cuts were applied to the updated parameters, and the final LSBG catalogue containing 23 790 LSBGs was created.

For training our classification models, we selected LSBGs from the LSBG catalogue as the positive class (label - 1) and the objects rejected in the third step (visual inspection) by Tanoglidis et al. (2021b) as the negative class (label - 0). The catalogues for the positive and negative classes are publicly available, and we used these catalogues to create our training dataset<sup>1</sup>. The selection of the artefacts and LSBGs for training was random, and after selection, we had 18 474 artefacts and 23 103 LSBGs. However, when we further inspected these LSBGs and artefacts, we found that there were 797 objects belonging to both classes. After conducting a thorough visual examination, we identified that these are, in fact, LSBGs that had been mistakenly categorized as artefacts in the publicly accessible artefact catalogue. However, we avoided these 797 objects from our training set to avoid contamination and ambiguity among classes during training. We generated multi-band cutouts for each object in the flexible image transport system (FITS) format using the cutout service provided in the DES public data archive. Each cutout corresponds to a  $67.32'' \times 67.32''$  ( $256 \times 256$  pixels) region of the sky and is centred at the coordinates of the object (LSBG or artefact). We resized the cutouts from their initial size to  $64 \times 64$  pixels to reduce the computational cost. The cutouts of  $g$ ,  $r$  and  $z$ -bands were stacked together to create the dataset for training the models. Examples of LSBGs and artefacts used for training the model are shown in Fig. 1. Our training catalogue contains 39 983 objects, out of which 22 306 are LSBGs and 17 677 are artefacts. Before training, we randomly split the full sample into a training set, a validation set and a test set, each consisting of 35 000, 2 500, and 2 483 objects, respectively.

### 3. Methodology

#### 3.1. Transformers and Attention

As mentioned in Sect. 1, the central idea behind every transformer architecture is attention. Before applying attention, the input sequence is transformed into three vectors in multi-head attention: query ( $Q$ ), key ( $K$ ), and value ( $V$ ). The dot product between the query and key vectors is used to obtain attention scores. The attention scores are then used to weight the value vector, producing a context vector that is a weighted sum of the value vectors. For our work, the vectors ( $Q$ ,  $V$  and  $K$ ) are identical, and this method is termed self-attention. This approach enables the transformer to model long-range dependencies and capture complex patterns in the input sequence. Mathematically, the attention function is defined as

$$\text{Attention}(Q, K, V) = \text{softmax}\left(\frac{QK^T}{\sqrt{d_k}}\right)V, \quad (4)$$

<sup>1</sup> <https://github.com/dtanoglidis/DeepShadows/blob/main/Datasets>

where  $Q, K, V$  are the query, key, and value vectors and  $d_k$  is the dimension of the vector  $K$ . The softmax function, by definition, is the normalised exponential function that takes an input vector of  $K$  real numbers and normalises it into a probability distribution consisting of  $K$  probabilities proportional to the exponential of the input numbers. The building blocks of our transformer models are layers applying self-attention and are termed transformer encoders. Please refer to Vaswani et al. (2017) for a detailed discussion on transformer encoders.

#### 3.2. LSBG Detection Transformer (LSBG DETR)

We implemented four transformer models that use a CNN backbone and self-attention layers to classify the labels, which we call LSBG DETR (LSBG detection transformers) models in general. The LSBG DETR architecture is inspired by transformer models from Thuruthipilly et al. (2022b), which explored diverse structures and hyperparameters to optimize classification performance. Each individual model is followed by a number indicating their chronological order of creation. The LSBG DETR models have an 8-layer CNN backbone to extract feature maps from the input image. The feature maps produced by the CNN backbone are then passed on to the transformer encoder layer to create an attention map that helps the transformer component focus on the most relevant features for classification. The transformer encoder layer has sub-components known as heads which parallelly apply the self-attention to the input vector split into smaller parts. Output generated by the transformer encoder is then passed on to a feed-forward neural network (FFN) layer to predict the probability of the input being an LSBG or not. Another point to be noted is that the transformers are permutation invariant; hence, we add positional encoding to address this issue and retain the positional information of features. For the LSBG DETR, we used fixed positional encoding defined by the function

$$PE_{(pos, 2i)} = \sin\left(\frac{pos}{12800^{\frac{2i}{d_{model}}}}\right), \quad (5)$$

$$PE_{(pos, 2i+1)} = \cos\left(\frac{pos}{12800^{\frac{2i}{d_{model}}}}\right), \quad (6)$$

where  $pos$  is the position,  $i$  is the dimension of the positional encoding vector, and  $d_{model}$  is the dimension of the input feature vector. We follow the positional encoding defined in Vaswani et al. (2017), and for a detailed discussion on positional encoding and its importance, we refer to Liutkus et al. (2021); Su et al. (2021); Chen et al. (2021). The general structure of the LSBG DETR is shown in Fig. 2. For a detailed discussion on the transformer models similar to LSBG DETR, we refer to Carion et al. (2020) and Thuruthipilly et al. (2022b).

#### 3.3. LSBG Vision

We have created four transformer models similar to the Vision Transformer (ViT) introduced by Google Brain (Dosovitskiy et al. 2021), which we call LSBG vision transformers (LSBG ViT) in general. Similar to LSBG DETR models, each individual model is followed by a number indicating their chronological order of creation. One of the main features of LSBG ViT models is that it does not use any convolutional layers to process the image, unlike LSBG DETR. In the ViT architecture, the input image is divided into fixed-size patches, which are flattened into a sequence of 1D vectors. Since the transformers are permutation invariant, the positional embedding is added to the patch embedding before they are fed into the transformer layers. The

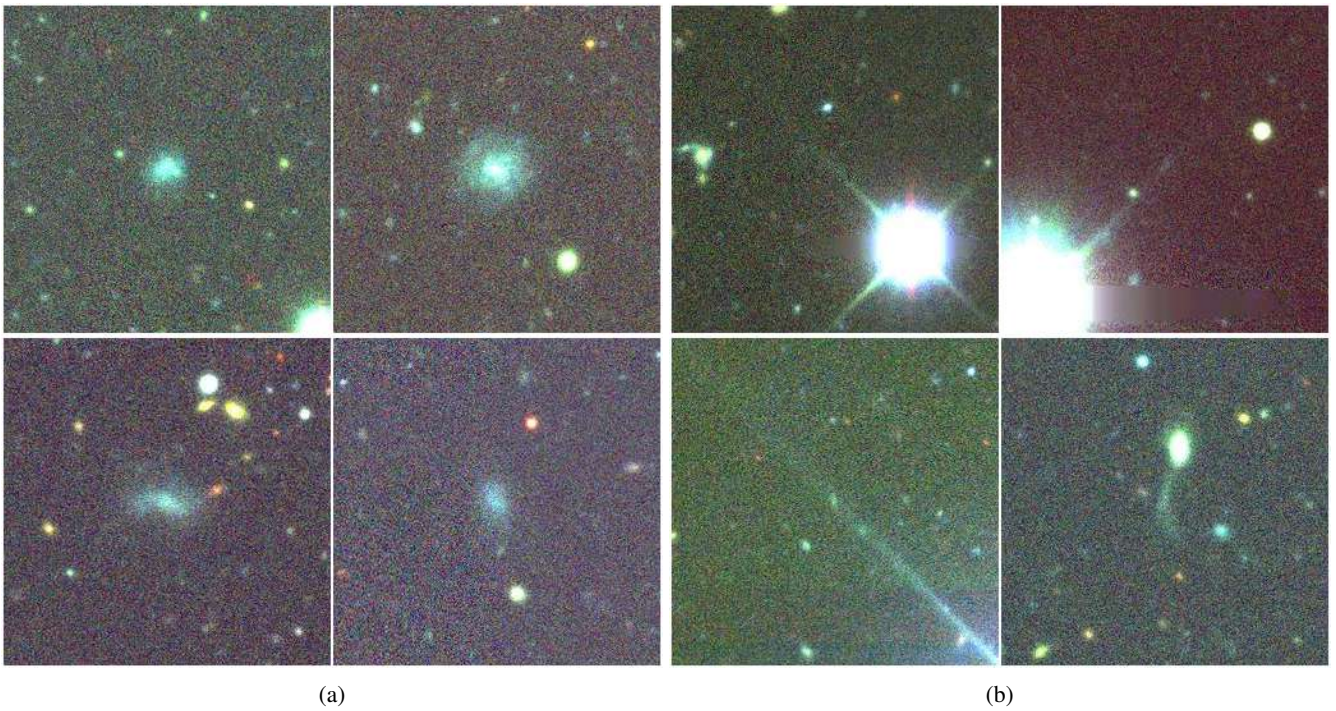


Fig. 1: Four examples of LSBGs (1a) and artefacts (1b) used in the training data. Each image of the LSBG and artefact corresponds to a  $67.32'' \times 67.32''$  region of the sky. Images were generated by combining the  $g$ ,  $r$  and  $z$  bands using APLpy package (Robitaille & Bressert 2012).

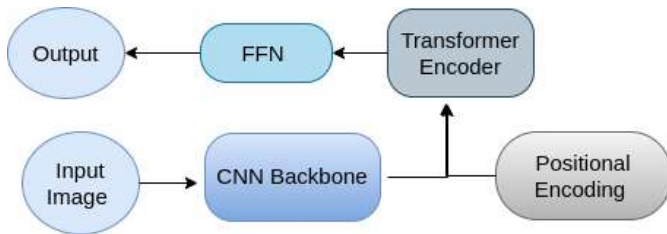


Fig. 2: Scheme of the general architecture of the Detection Transformer (LSBG DETR) taken from Thuruthipilly et al. (2022b). The extracted features of the input image by the CNN backbone are combined with positional encoding and passed on to the encoder layer to assign attention scores to each feature. The weighted features are then passed to the feed-forward neural network (FFN) to predict the probability.

positional embedding is typically a fixed-length vector that is added to the patch embedding, and it is learned during training along with the other model parameters. The combined 1-D sequence is then passed through a stack of transformer layers. An additional learnable (class) embedding is affixed to the input sequence, which encodes the class of the input image. This class embedding for each input is calculated by applying self-attention to positionally embedded image patches. Output from the class embedding is passed on to a multi-layer perceptron (MLP) head to predict the output class. A schematic diagram of the Vision transformer is shown in Fig. 3. For a detailed discussion on ViT models, please refer to Dosovitskiy et al. (2021).

### 3.4. Training

All of the LSBG DETR and LSBG ViT models were trained with an initial learning rate of  $\alpha = 10^{-4}$ . We used the exponen-

tial linear unit (ELU) function as the activation function for all the layers in these models (Clevert et al. 2016). We initialise the weights of our model with the Xavier uniform initialiser (Glorot & Bengio 2010), and all layers are trained from scratch by the ADAM optimiser with the default exponential decay rates (Kingma & Ba 2015). We have used the early stopping callback from Keras<sup>2</sup> to monitor the validation loss of the model and stop training once the loss was converged. The models LSBG DETR 1 and 4 had 8 heads and were trained for 150 and 93 epochs, respectively. Similarly, the LSBG DETR 2 and 3 had 12 heads and were trained for 134 and 105 epochs, respectively. Coming to the LSBGS ViT models, the hyperparameters we varied were the size of the image patches, the number of heads and the number of transformer encoder layers. The hyperparameters for the all the LSBG DETR models were customized based on the results from Thuruthipilly et al. (2022b), which extensively investigated the hyperparameter configurations of DETR models. When it comes to the LSBG vision transformer models, we maintained the hyperparameters from the LSBG DETR models such as learning rate, and batch size, except for adjustments in image patch size, the count of attention heads, and the number of transformer encoder layers. We varied these parameters and the four best models are presented in Table 1. In the spirit of reproducible research, our code for LSBG DETR and LSBG ViT is publicly available<sup>3</sup>.

### 3.5. Ensemble Models

We had two classes of transformers (LSBG DETR and LSBG ViT) with four models in each class, and we used an ensemble model of these four models for each class to look for new LS-

<sup>2</sup> <https://keras.io/api/callbacks>

<sup>3</sup> <https://github.com/hareesht23/>

Table 1: Table showing the name of the model, size of the image patches (s), number of heads (h), number of transformer encoder layers (T) and the number of epochs taken to train (e) the four vision models in chronological order of creation.

Model Name	s	h	T	e
LSBG VISION 1	4	12	4	55
LSBG VISION 2	4	12	8	55
LSBG VISION 3	6	12	4	67
LSBG VISION 4	6	16	8	67

BGs from DES DR1. Ensemble models in deep learning refer to combining multiple models to create a single model that performs better than the individual models. The idea behind ensemble models is to reduce the generalisation error and increase the stability of the system by taking into account multiple sources of information. Various kinds of ensemble learning exist in the literature, and they have been found helpful in a broad range of machine learning problems (Wang et al. 2022). For a detailed review of ensemble methods, please refer to Domingos & Hulten (1999) and Dietterich (2000). One of the easiest and most common ensemble methods is model averaging. In model averaging, multiple models are trained independently on the same training data, and the outputs of the models are averaged to make the final prediction. One of the main advantages of model averaging is that it is computationally efficient and does not require any

additional training time. It also allows the use of different types of model architectures and can take advantage of their strengths and weaknesses and improve overall performance. Here we use averaging to create the ensemble models for LSBG DETR and LSBG ViT.

### 3.6. Sérsic fitting

The candidates identified independently by both LSBG DETR and LSBG ViT ensemble models were subjected to a single component Sérsic fitting using Galfit (Peng et al. 2002). This was done to re-estimate the  $\bar{\mu}_{eff}$  and  $r_{1/2}$  values of our LSBG candidates that we initially used for our sample selection. We employed a single-component Sérsic fitting method to align with the LSBG search methodology of Tanoglidis et al. (2021b), who also utilized a similar approach. However, we also note that Sérsic fitting does not always capture the full light from a galaxy.

We used the magnitude (MAG\_AUTO) and radius (FLUX\_RADIUS) values from the gold catalogue as an initial guess for the Galfit procedure. Moreover, the Sérsic index ( $n$ ) and axis ratio ( $q$ ) were initialised to be at a fixed value of 1 and were allowed to vary only within the range of  $0.2 < n < 4.0$  and  $0.3 < q \leq 1.0$ , respectively. A similar fitting procedure was done for both the  $g$ -band and  $i$ -band images of our sample. After the fitting, we excluded all the sources with poor/failed fits with either a reduced  $\chi^2 > 3$  or if their Galfit magnitude estimates

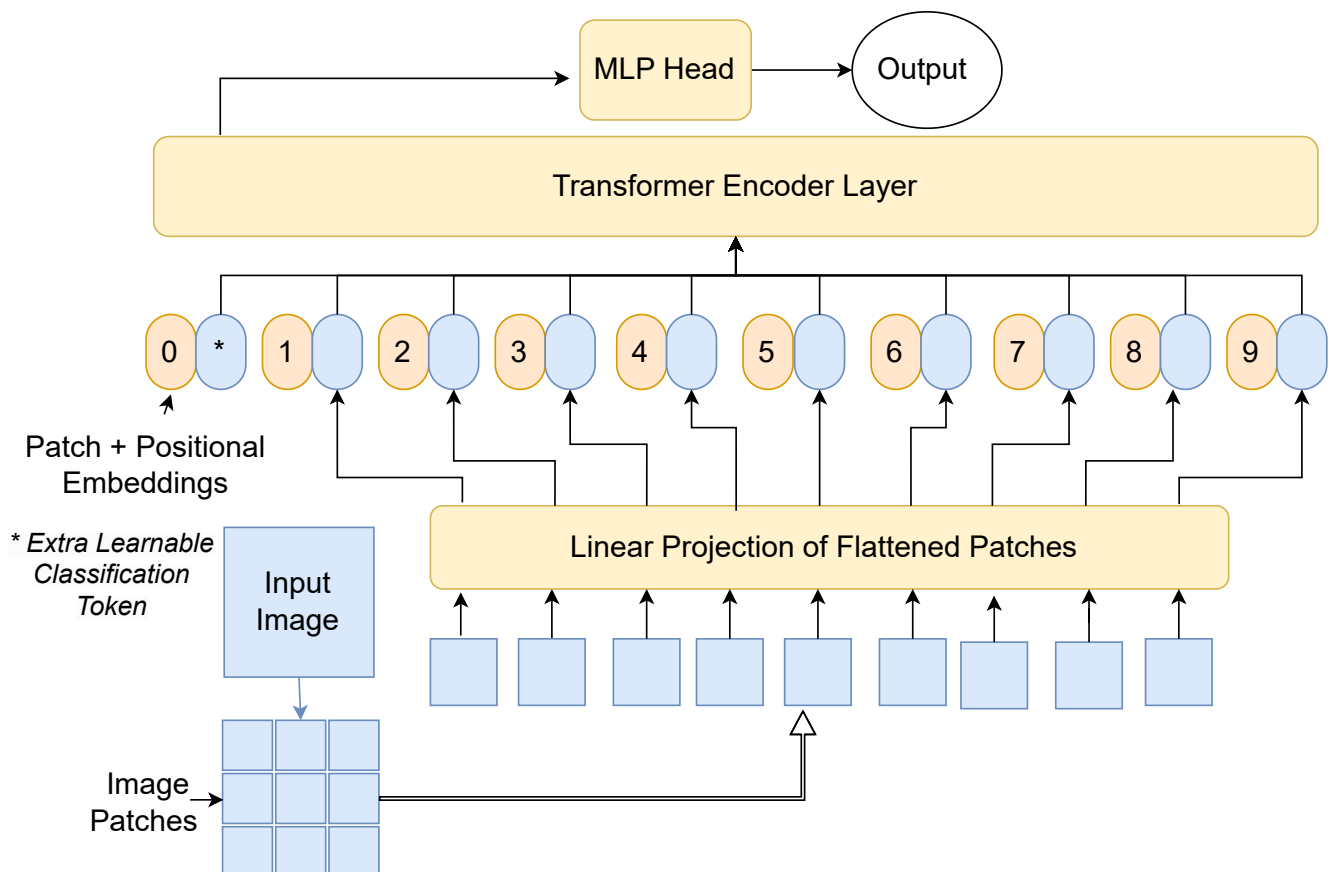


Fig. 3: Scheme of the general architecture of the LSBG vision transformer (LSBG ViT). The input image is split into small patches and flattened into a sequence of 1D vectors and combined with positional encoding. The numbered circular patches represent the position encoding, and the counterpart represents the flattened 1-D sequence of the image patches. The combined 1-D sequence is passed to the transformer layers. The extra learnable class embedding has encoded the class of the input image after being updated by self-attention and passed it on to an MLP head to predict the output.

diverge from their initial `MAG_AUTO` values by more than one mag. We have also excluded the cases where the estimated  $n$  and  $q$  values do not converge and are on the edge of the range specified above. For the remaining galaxies, we re-applied our  $g$ -band sample selection criteria of  $\bar{\mu}_{eff} > 24.2$  mag arcsec<sup>-2</sup> and  $r_{1/2} > 2.5''$ , following Tanoglidis et al. (2021b). The  $\bar{\mu}_{eff}$  values were calculated using the relation given by Eq. 7:

$$\bar{\mu}_{eff} = m + 2.5 \times \log_{10}(2\pi r_{1/2}^2), \quad (7)$$

where  $\bar{\mu}_{eff}$  is the mean surface brightness within the effective radius,  $m$  is the total magnitude and  $r_{1/2}$  is the half-light radius in a specific band estimated from `Galfit`. For all our measurements, we also applied a foreground Galactic extinction correction using the Schlafly et al. (1998) maps normalised by Schlafly & Finkbeiner (2011) and a Fitzpatrick (1999) dust extinction law.

### 3.7. Visual Inspection

Only the candidates identified independently by LSBG DETR and LSBT ViT ensemble models and passed the selection criteria for being an LSBG with the updated parameters from the `Galfit` were considered for visual inspection. This refined sample was subjected to visual inspection by two authors independently. Candidates identified as LSBG by both authors were treated as confident LSBGs, and candidates identified as LSBG by only one author were reinspected together to make a decision. Since visual inspection is time-consuming, we only resorted to it at the last step and tried as much to reduce the number of candidates shortlisted for visual inspection.

To aid in visual inspection, we used two images for every candidate. We generated images enhancing the low surface brightness features using the `APLpy` package (Robitaille & Bressert 2012) and images downloaded from the DESI Legacy Imaging Surveys Sky Viewer (Dey et al. 2019). Furthermore, the  $g$ -band Sérsic models from `Galfit` were also used to visually inspect the quality of the model fitting. Each candidate was then categorised into three classes based on the `Galfit` model fit and the images: LSBG, non-LSBG (Artifacts), or misfitted LSBGs. If the model of the galaxy was fitted correctly and the candidate showed LSBG features, it was classified as an LSBG. If the candidate shows LSBG features but does not fit correctly, we classify it as a misfitted LSBG. Finally, if the candidate does not have features of an LSBG, we classify it as an artefact or non-LSBG.

### 3.8. Metrics for comparing models

Here, we use accuracy, true positive rate (TPR), false positive rate (FPR) and area under the receiver operating characteristic (AUROC) curve as the metrics to compare the performance of the created transformer models. The classification accuracy of a model is defined as:

$$\text{Accuracy} = \frac{TP + TN}{TP + FP + TN + FN}, \quad (8)$$

where TP is the number of true positives, TN is the number of true negatives, FP is the number of false positives, and FN is the number of false negatives. Since identifying LSBGs with less contamination is our primary focus, rather than the overall accuracy of the classifier, TPR and FPR are more informative metrics for evaluating the classifier's performance. The TPR is the ratio of LSBGs identified by the model to the total number of LSBGs,

which can be expressed as

$$TPR = \frac{TP}{TP + FN}. \quad (9)$$

In the literature, sensitivity is another term used to represent the True Positive Rate (TPR), and it measures how well a classifier detects positive instances (in this case, LSBGs) from the total number of actual positive instances in a dataset. Similarly, FPR can be considered a contamination rate because it measures how often the classifier incorrectly classifies negative instances as positive. FPR is defined as

$$FPR = \frac{FP}{FP + TN}. \quad (10)$$

All the quantities defined above are threshold dependent and vary as a function of the chosen probability threshold. By constructing the receiver operating characteristic curve (ROC) and finding the AUROC, one could define a threshold-independent metric for comparing the models. The ROC curve is constructed by plotting the true positive rate (TPR) and false positive rate as a function of the threshold. The area under the ROC curve (AUROC) measures how well a classifier distinguishes between classes and is a constant for the model, unlike the accuracy, which varies with a threshold. If the AUROC is 1.0, the classifier is perfect with TPR = 1.0 and FPR = 0.0 at all thresholds. A random classifier has an AUROC  $\sim 0.5$ , with TPR almost equal to FPR for all thresholds.

## 4. Results

### 4.1. Model performance on the testing set

We have created four models of each transformer, namely LSBG DETR and LSBG ViT, with different hyperparameters to generalise our results for both transformers. Each model was implemented as a regression model to predict the probability of an input being an LSBG, and we set 0.5 as the threshold probability for classifying an input as LSBG. Further, we use an ensemble of the four models as the final model for LSBG DETR and LSBG ViT. Table 1 describes the architecture, accuracy and AUROC of all the models, including the ensemble models on the test dataset, as mentioned in section 2.3.

Table 2: Table comprising the architecture, accuracy, true positive rate (TPR), false positive rate (FPR) and AUROC of all the models in chronological order of creation.

Model name	Accuracy (%)	TPR	FPR	AUROC
LSBG VISION 1	93.55	0.97	0.12	0.980
LSBG VISION 2	93.79	0.97	0.11	0.980
LSBG VISION 3	93.47	0.97	0.11	0.981
LSBG VISION 4	93.51	0.97	0.11	0.980
LSBG VISION Ensemble	<b>93.75</b>	<b>0.97</b>	<b>0.11</b>	<b>0.983</b>
LSBG DETR 1	94.36	0.97	0.09	0.982
LSBG DETR 2	94.28	0.96	0.08	0.980
LSBG DETR 3	94.36	0.96	0.08	0.982
LSBG DETR 4	94.24	0.95	0.07	0.982
LSBG DETR Ensemble	<b>94.60</b>	<b>0.96</b>	<b>0.07</b>	<b>0.984</b>

As mentioned earlier, the more insightful metrics are the true positives (TPR) and the false positives (FRP) rather than overall accuracy. These metrics can be visualised using a confusion matrix, which is shown in Fig. 4, for the ensemble models using a

threshold of 0.5. The LSBG DETR ensemble had a TPR of 0.96 and an FPR of 0.07, indicating that the LSBG DETR ensemble model can accurately identify 96% of all LSBGs in the DES data, with an estimated 7% contamination rate in the predicted sample. Similarly, the LSBG ViT Ensemble model can identify 97% of all the LSBGs in DES but with 11% contamination.

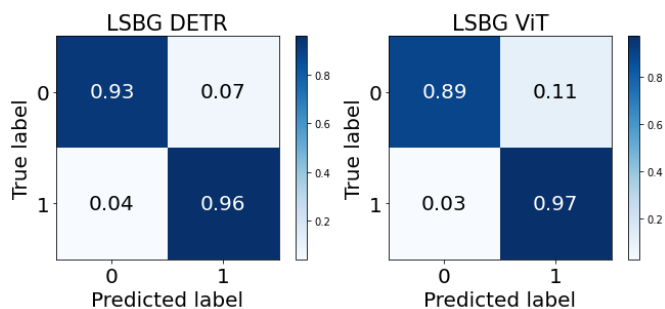


Fig. 4: Confusion matrix of LSBG DETR and LSBG ViT models plotted for a threshold = 0.5. Class 0 represents the artefacts, and Class 1 represents the low surface brightness galaxies.

The receiver operator characteristic (ROC) curve of the LSBG DETR and LSBG ViT ensemble models are shown in Fig. 5. In terms of accuracy and AUROC, the LSBG DETR models performed slightly better than the LSBG ViT models. It is clear from Fig. 5 that both the ensemble models have a TPR  $\sim 0.75$  even for a high threshold such as 0.9. Indicating that both the ensemble models can confidently identify around  $\sim 75\%$  of all the LSBGs in DES and assign these candidates with a probability greater than 0.9.

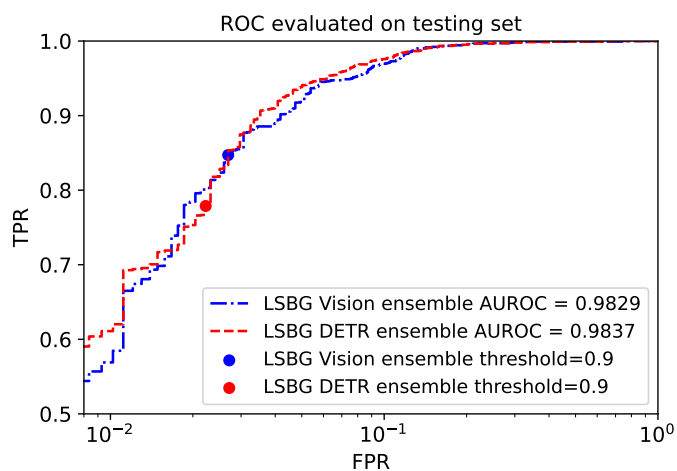


Fig. 5: Receiver operating characteristic (ROC) curve of the ensemble models. The red and blue lines represent the variation of FPR and TPR as a function of the threshold for LSBG DETR and LSBG Vision ensembles, respectively. The red and blue points mark the TPR and FPR for a threshold = 0.9.

#### 4.2. Search for LSBGs in the full coverage of DES

Since the LSBG DETR model and the LSBG ViT model have different architectures and feature extraction principles, we regard the ensemble models of these two as separate independent transformer classifiers. In order to search for new LSBGs from DES, we employed the transformer ensemble model on the 419 782 objects that satisfied the selection criteria defined

in section 2.2. The candidates scoring above the threshold probability of 0.5 were catalogued as potential LSBG candidates. The LSBG DETR ensemble classified 27 977 objects as LSBGs, among which 21 005 were already identified by Tanoglidis et al. (2021b). Similarly, the LSBG ViT ensemble classified 30 508 objects as LSBGs, among which had 21 396 LSBGs common with the sample identified by Tanoglidis et al. (2021b). So finally, 6 972 and 9 112 new candidates were classified as potential LSBGs by the LSBG DETR and LSBG ViT ensembles, respectively. However, only the 6 560 candidates identified by both the ensemble models independently were considered for further analysis to reduce the false positives. Since there is a possibility that there might be duplicates of the same candidates existing in the selected sample, we ran an automated spatial crossmatch to remove duplicate objects separated by  $< 5''$ . The origin of these duplicates can be traced back to the fragmentation of larger galaxies into smaller parts by SourceExtractor. After removing the duplicates, the number of potential LSBG candidates reduced from 6 560 to 6 445. As discussed in Sect. 3.6, these candidates were subjected to single component Sérsic model fitting using Galfit.

During the Galfit modelling, 999 candidates had failed fits and were consequently removed from the sample since our objective is to produce a high-purity sample with accurate Sérsic parameters. We visually inspected these unsuccessful fits and found that in most cases the presence of a very bright object near the candidate was the cause of the poor Sérsic fit. Of the remaining 5 446 candidates, 4 879 passed the  $\bar{\mu}_{eff}$  and  $r_{1/2}$  selection criteria outlined in Sect. 2.2 with the updated parameters. These 4 879 candidates were inspected visually to identify the genuine LSBGs. After independent visual inspections by the authors, 4 190 candidates were classified as LSBGs and 242 candidates were found to be non-LSBGs. During visual inspection, 447 candidates were found to be possible LSBGs with unreliable measurements from Galfit. These candidates are excluded from our final sample, and here we only report on the most confident candidates that were identified as LSBGs during visual inspection. After correcting for the Galactic extinction correction, our final sample reduced to 4 083 new LSBGs from DES DR1. The schematic diagram showing the sequential selection steps used to find the new LSBG sample is shown in Fig. 6. A sample catalogue comprising the properties of the newly identified LSBGs is shown in table 3, and some examples of the new LSBGs that we have found are plotted in Fig. 7.

The distribution of the  $r_{1/2}$ ,  $\bar{\mu}_{eff}$ , Sérsic index ( $n$ ), and axis ratio ( $q$ ) of the new sample of LSBGs is plotted in Fig. 8. The majority of the LSBGs in this new sample have  $r_{1/2} < 7''$ , and  $\bar{\mu}_{eff} < 26$  mag arcsec $^{-2}$ . The Sérsic index of the new LSBG sample predominantly lies between 0.5 and 1.5 and has a median value of 0.85. This pattern is similar to the trend identified by Poulain et al. (2021) in the case of dwarf ellipticals, suggesting that a significant portion of the LSBGs sample could be comprised of such sources. In the case of the axis ratio, the new LSBG sample has a median axis ratio of 0.72 and has a distribution lying in the range of 0.3 to 1. The median value of 0.72 suggests that most galaxies in this sample have a slightly flattened or elongated shape. A detailed discussion of the properties of the new LSBGs identified in this work and their comparison with LSBGs identified by Tanoglidis et al. (2021b) is presented in Sect. 5.



Table 3: Sample of new LSBGs identified in this work.

COADD_ID	RA (deg)	DEC (deg)	$g_{gf}$	$g_{cor}$	$\bar{\mu}_{g,eff\_gf}$ (mag arcsec <sup>-2</sup> )	$r_{g1/2}$ (arcsec)	n	q	$\log_{10}(\Sigma_{star})$ ( $M_{\odot} \text{ kpc}^{-2}$ )	$\chi_{vg}^2$	$i_{gf}$	$i_{cor}$	$\bar{\mu}_{i,eff\_gf}$ (mag arcsec <sup>-2</sup> )	$r_{i1/2}$ (arcsec)	$\chi_{vi}^2$
61456395	29.7062	-60.4882	19.06	18.97	25.41	9.41	2.17	0.62	5.86	1.06	18.72	18.67	25.37	10.86	1.03
61508029	29.925	4.60483	19.84	19.67	24.33	3.43	0.72	0.85	6.82	1.03	19.27	19.19	23.52	3.06	0.99
61580602	30.3125	-58.1927	18.89	18.83	24.56	5.99	1.5	0.82	6.87	1.02	18.07	18.04	23.72	5.93	1.02
61638403	29.9539	4.75811	20.02	19.87	24.28	3.84	0.74	0.54	6.52	1.04	19.61	19.53	23.62	3.45	1
61638933	29.4862	4.74468	19.2	19.06	24.24	4.59	0.93	0.79	6.82	0.98	18.7	18.63	23.38	3.89	0.99
61712539	30.2824	5.28992	19.67	19.53	24.26	4.57	1.01	0.52	6.58	1.01	19.47	19.4	23.2	3.07	1.03
61766250	30.1112	-9.24769	20.76	20.69	26.29	7.8	1.47	0.42	5.87	1.13	20.19	20.15	25.2	6.15	1.1
62011325	29.9449	-6.78979	21.6	21.51	25.91	3.17	0.5	0.84	6.27	1.02	20.8	20.76	25.21	3.31	1
62053525	29.8595	-16.8586	19.87	19.8	24.24	3.49	0.87	0.73	6.81	1.03	19.32	19.29	23.41	3.06	1.02
62071354	29.8342	-17.1604	20.53	20.46	24.47	3.01	0.84	0.66	6.71	0.99	19.91	19.87	23.65	2.75	0.99
62222622	29.5063	-13.3511	20.84	20.79	24.88	2.68	0.68	0.91	7.24	1.02	19.97	19.94	22.96	1.66	1.05
62371677	29.6675	-5.35506	19.7	19.62	24.25	3.54	0.79	0.84	6.97	1.05	19	18.96	23.32	3.2	1.03
62646182	30.4643	-24.0018	18.46	18.4	24.44	6.88	1.19	0.83	6.77	1	17.98	17.95	23.59	5.8	0.97
62830903	29.9594	-28.8656	20.11	20.07	24.35	2.94	0.71	0.91	7.56	1.03	19.01	18.99	22.44	2.03	1.04
62840965	30.1905	-6.18018	20.18	20.1	24.35	2.74	0.76	0.98	7.35	1.01	19.22	19.18	22.85	2.14	1
63037584	28.9741	-59.5261	19.46	19.39	24.4	6.33	0.9	0.38	6.31	1.01	18.88	18.85	23.99	6.81	1.01
63097874	29.3755	-61.1452	20.6	20.51	24.87	3.08	1.02	0.85	6.58	1.02	20.29	20.25	23.86	2.23	1.02
63113174	29.1535	-61.4326	18.81	18.72	24.78	6.73	0.8	0.86	6.47	1	18.52	18.47	24.15	5.76	0.99
63262376	30.2929	-24.9787	21.48	21.43	26.1	3.92	0.98	0.73	6.18	1.03	20.62	20.6	25.35	4.12	1.04
63527438	30.1134	-4.56234	18.8	18.73	24.51	6.72	0.42	0.68	6.2	1.02	18.68	18.65	24.37	6.63	0.99
63716543	30.0657	-39.5446	20.58	20.52	25.1	3.73	1.16	0.74	6.67	1.02	19.84	19.81	24.01	3.17	1.01
63922768	29.5244	-32.7958	18.41	18.35	24.6	7.62	1.61	0.83	6.59	1.08	18.06	18.03	23.87	6.37	1.04
64480503	29.4619	-23.0107	18.98	18.94	24.33	5.05	0.91	0.86	6.81	1.04	18.5	18.48	23.54	4.39	1
64560481	30.0521	-5.09785	18.18	18.1	24.36	7.21	1.17	0.91	6.86	1.06	17.66	17.62	23.49	6.14	1.01
64697654	29.5818	-8.50243	18.36	18.28	24.25	6.46	1	0.87	6.81	0.97	17.87	17.83	23.53	5.78	0.96
64773733	29.0012	-50.2462	19.39	19.32	24.7	5.13	1.4	0.8	6.66	1.03	18.94	18.91	23.78	4.13	1.01
64868340	29.3394	-23.8729	19.43	19.38	24.2	3.72	0.86	0.93	7.63	1.02	18.36	18.34	22.23	2.47	1.26

**Notes.** 'COADD\_ID' is the unique id of the source, and 'RA' and 'DEC' gives the sky coordinates of the source as estimated from DES Y3 gold catalogue (Sevilla-Noarbe et al. 2021). Columns ' $g_{gf}$ ', ' $g_{cor}$ ', ' $\bar{\mu}_{g,eff\_gf}$ ', and ' $r_{g1/2}$ ' represents the magnitude in  $g$  band, the  $g$  band magnitude after correcting for Galactic extinction, mean surface brightness and the half-light radius for the  $g$ -band fitting using GalFit, respectively. The columns 'n', 'q', and ' $\log_{10}(\Sigma_{star})$ ' represent the Sérsic index, axis ratio, and the stellar mass density, respectively. Column ' $\chi_{vg}^2$ ', represent the reduced chi-square value for the  $g$ -band fitting using GalFit. Similarly, columns ' $i_{gf}$ ', ' $i_{cor}$ ', ' $\bar{\mu}_{i,eff\_gf}$ ', ' $r_{i1/2}$ ', and ' $\chi_{vi}^2$ ' represents the magnitude in  $i$  band, the  $i$  band magnitude after correcting for Galactic extinction, the mean surface brightness, the half-light radius and the reduced chi-square value for the  $i$  band fitted using GalFit, respectively.

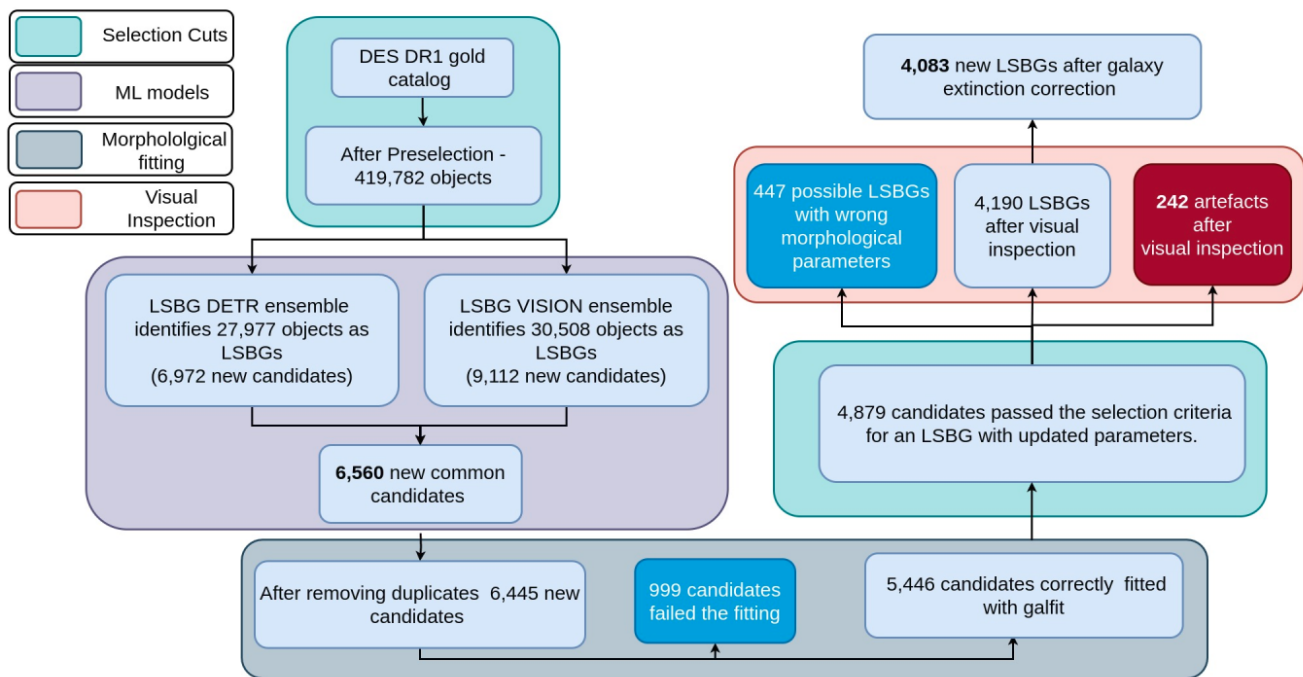


Fig. 6: Schematic diagram showing the sequential selection steps used to find the new LSBG sample.

## 5. Discussion

### 5.1. Transformers as LSBG Detectors

In this study, we introduce the use of transformers as a classifier model for finding the undiscovered LSBGs in DES. Currently, in the literature, one of the reported deep-learning-based models for classifying LSBGs and artefacts is a CNN model named DeepShadows created by Tanoglidis et al. (2021a). They used the catalogue of LSBGs and artefacts identified from DES reported in Tanoglidis et al. (2021b) to generate the training data. The DeepShadows model achieved an accuracy of 92% in classifying LSBGs from artefacts and had a true positive rate of 94% with a threshold of 0.5. Moreover, the DeepShadows model also achieved an AUROC score of 0.974 on this training dataset. However, the DeepShadows was not applied to the complete DES data and checked how it would perform. Nevertheless, DeepShadows was the first deep-learning model to classify LSBGs and artefacts. In addition, Tanoglidis et al. (2021a) also showed that the DeepShadows was a better classifier than the support vector machine or random forest models. However, in our work, all of our transformer models were able to surpass the DeepShadows model in every metric individually, which can be seen from Table 2. Namely, in their respective classes, LSBG DETR 1 and LSBG ViT 2 had the highest accuracies (94.36% and 93.79%), respectively.

Earlier searches for LSBGs have used semi-automated methods such as pipelines based on `imfit` by Greco et al. (2018) or simple machine-learning models such as SVMs by Tanoglidis et al. (2021b). However, the success rate of these methods was very low, and the final candidate sample produced by these methods had around 50% false positives, which had to be removed by visual inspection. Here we explore the possibilities of transformer architectures in separating LSBGs from artefacts. We used two independent ensemble models of LSBG DETR and LSBG ViT models and single component Sérsic model fitting to filter the LSBG candidates. Our final sample contained only

~ 5% as non-LSBGs, which is a significant improvement compared to the previous methods in the literature. Following the definition of an LSBG as described in Tanoglidis et al. (2021b), we identified 4083 new LSBGs from DES DR1, increasing the number of identified LSBGs in DES by 17%. Our results highlight the significant advantage of using deep-learning techniques to search for LSBGs in the upcoming large-scale surveys.

To have more insights into the fraction of false positives from our method, we checked the performance of these models during training. We encountered around 7% and 11% of artefacts from the LSBG DETR ensemble and LSBG ViT sample, respectively, during training on the test dataset. However, using a combination of these models, we reduced the artefact fraction to less than 5% during visual inspection. Most of the non-LSBGs we encountered during the visual inspection were faint compact objects that blended in the diffuse light from nearby bright objects. We use the term 'non-LSBG' instead of artefacts here because, during the visual inspection, we classified some potential LSBGs as non-LSBG; these are objects for which the  $g$ -band images had instrumental artefacts or lack of sufficient signal in the  $g$ -band. Since the machine learning model intakes three bands as input ( $g$ ,  $r$  and  $z$ ), this suggests that the model was able to study and generalise the nature of LSBGs in each band and was able to predict if it is an LSBG or not based on the signal from the other bands. However, since we define LSBGs based on their  $g$ -band surface brightness and radius in this work, we classified the galaxies without reliable  $g$ -band data as non-LSBGs. Some non-LSBGs we encountered during the visual inspection are shown in Fig. 9 and Fig. 10. With the upcoming surveys of deeper imaging, these galaxies might be classified as LSBGs which might further reduce the non-LSBGs in our candidate sample.

One another fact to notice when discussing the non-LSBGs from the candidate sample is that some of the candidates identified as LSBGs by the ensemble models (567 out of 5446) did not meet the selection criteria of being an LSBG after being fitted with `Galfit`. These galaxies had  $r_{1/2}$  ranging from  $2''$  to

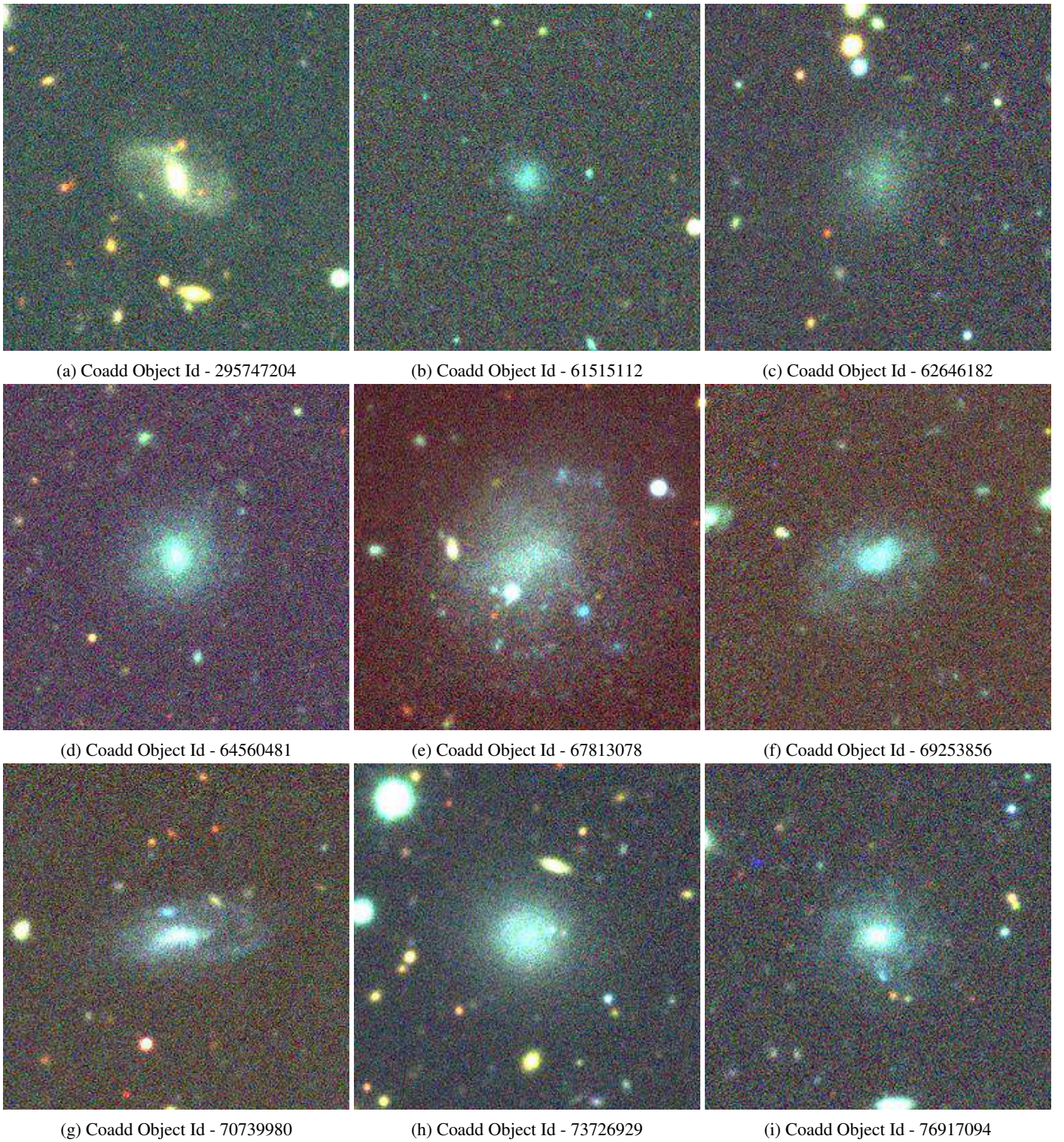


Fig. 7: Cutouts of 9 confirmed new LSBGs after visual inspection. The unique identification number (co object id) for each galaxy in DES DR1 is given below each image. The images were generated by combining the  $g, r$  and  $z$  bands using APLpy package (Robitaille & Bressert 2012), and each image corresponds to a  $67.32'' \times 67.32''$  region of the sky with the LSBG at its centre.

$20''$ , with a median of  $3.85''$ , which is similar to the new LSBG sample we found. However, the majority of these galaxies have a mean surface brightness between  $24.0 - 24.2 \text{ mag arcsec}^{-2}$ , with a median of  $24.16 \text{ mag arcsec}^{-2}$ . This suggests that the machine learning model understood the criteria for angular size for LSBGs during its training, but it did not learn the strict condi-

tion about the surface brightness. This situation is similar to a human expert analysing a galaxy image to determine whether it is an LSBG or not. Features such as the size of the galaxy are easily identifiable to the human eye. However, determining the surface brightness accurately with only the human eye would be challenging, and there may be possible errors near the threshold

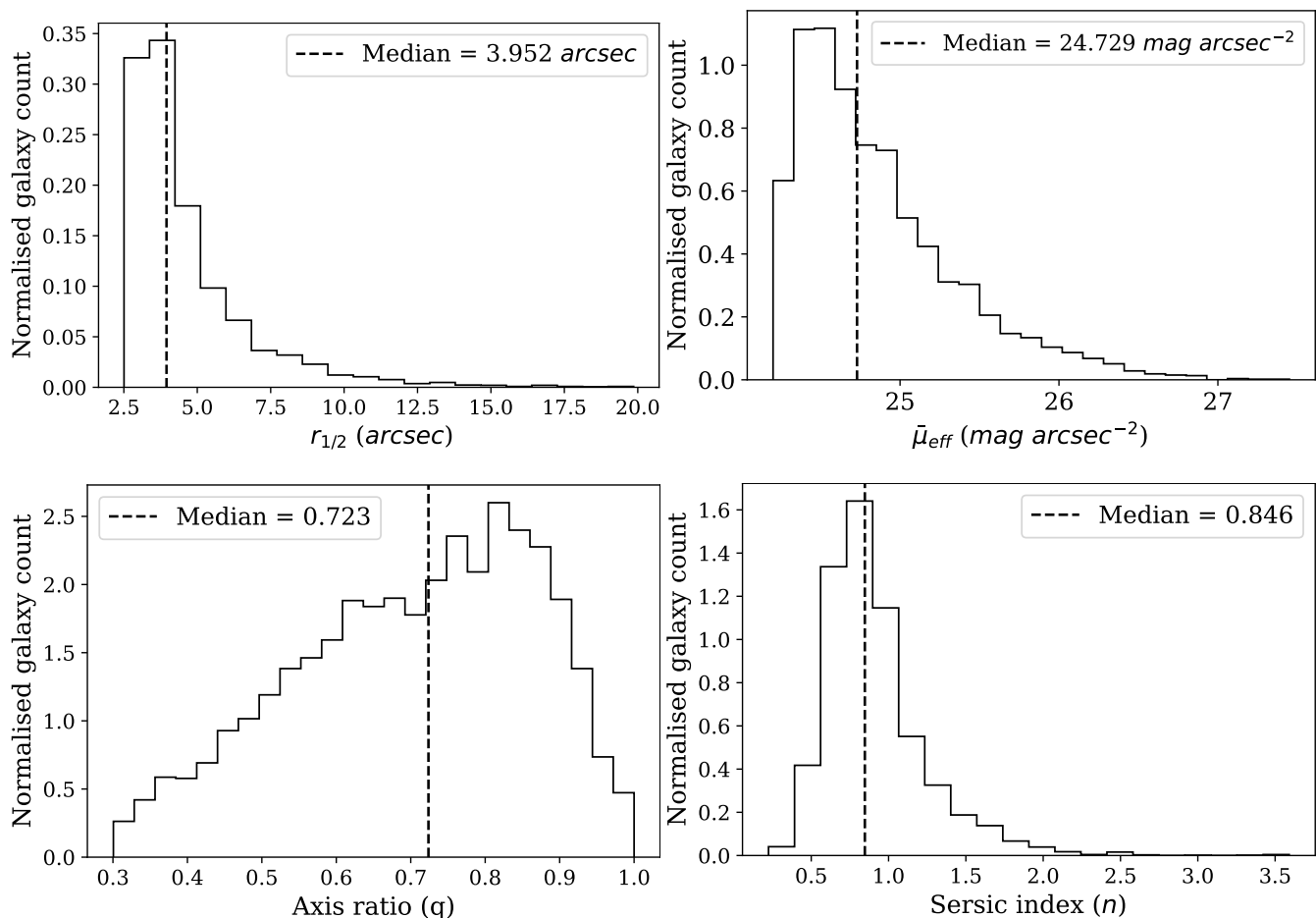


Fig. 8: Normalised distribution of half-light radius (top left panel), mean surface brightness (top right panel), Sérsic index (bottom left panel) and axis ratio (bottom right panel) of the new sample of LSBGs. The dashed line shows the median of the distribution

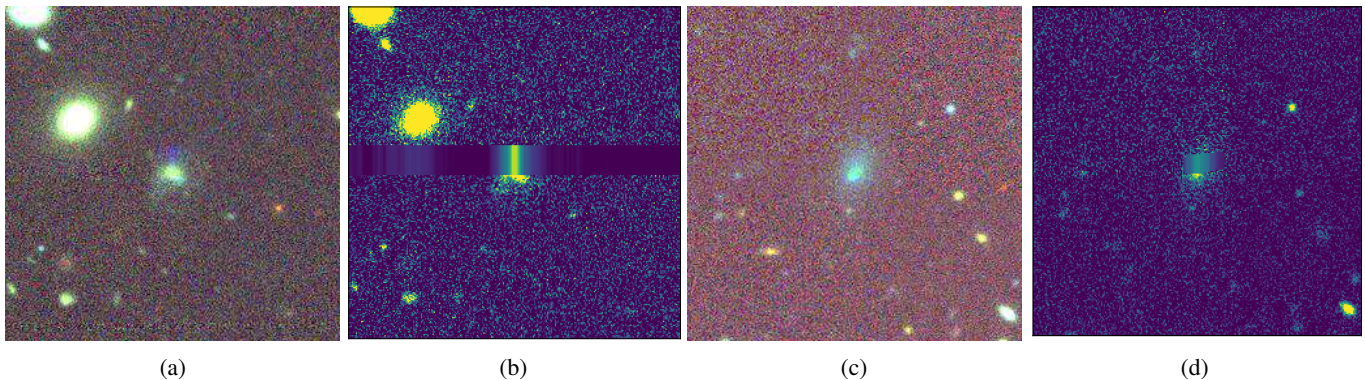


Fig. 9: Examples of candidates (Coadd object id - 149796289 and 374192591) classified as non-LSBGs during visual inspection because of glitches in the g-band near the galaxy. The panels (a) and (c) show the RGB image created using the  $g$ ,  $r$  and  $z$  bands with APLpy package (Robitaille & Bressert 2012). The panels (b) and (d) show the image in the  $g$  band. Each image corresponds to a  $67.32'' \times 67.32''$  region of the sky with the candidate at its centre.

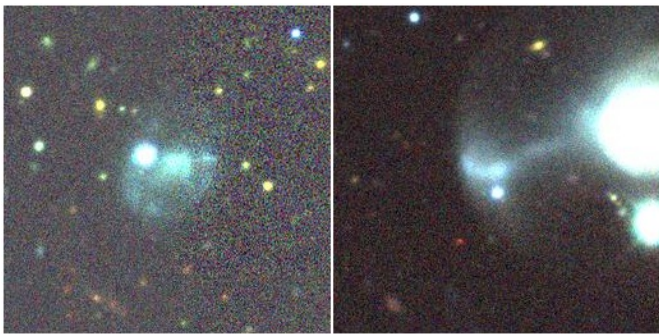
region, similar to our machine learning model. So one could say that the machine learning model is behaving approximately like a human visual expert.

Judging from the performance of our model on the training data, we cannot assert that we have discovered all the possible existing LSBGs from the DES DR1. As we can see from Fig. 4, the TP rate for the individual ensemble models were 0.96 and

0.97, respectively. This means that the model has not found all the possible LSBGs and a minor fraction of LSBGs is yet to be found in DES DR1. Moreover, to reduce the FPR and the burden during the visual inspection, we have only visually inspected the candidates identified commonly by both the ensemble models and passed the criteria for correctly fitting by Galfit.



(a) Coadd object id - 251235955 (left) and 99585243 (right)



(b) Coadd object id - 125313682 (left) and 113818243 (right)

Fig. 10: Examples of candidates classified as non-LSBG during visual inspection because of lack of sufficient signal in the  $g$ -band (a) are shown in the top panel. Candidates classified as non-LSBG during visual inspection because of being artefacts are shown in the lower panel (b). The RGB images are created using the  $g$ ,  $r$  and  $z$  bands with APLpy package (Robitaille & Bressert 2012). Each image corresponds to a  $67.32'' \times 67.32''$  region of the sky with the candidate at its centre.

One of the notable things about the models in this work is that we are using two different ensemble models, each having four models in the ensemble. As we mentioned earlier, each ML model can be considered equivalent to a human inspector, and the ensemble models help balance out the disadvantages of the other models in the ensemble. A closer look at the individual probability distribution of these modes shows that there are 310 candidates among the 4 083 confirmed LSBG candidates, which had a probability of less than 0.5 for at least one model among the individual models. However, since we used an average ensemble model, we were able to identify these LSBG by balancing out the probability, which shows the advantages of using an ensemble model over a single model.

Here, we use the visual inspection as the final step to confirm the authenticity of an LSBG detected by the models. However, it is essential to acknowledge the potential for human bias during the visual inspection, which can impact the accuracy and reliability of the results. For example, during the visual inspection, the visual inspectors disagreed on labelling approximately 10% of the candidate sample. Most of these galaxies had a mean surface brightness greater than  $25.0 \text{ mag arcsec}^{-2}$ , which suggests that even for human experts, it is challenging to characterise extremely faint LSBGs. However, with better imaging, this might change, but we must acknowledge that there will always be some human bias and error associated with human inspection. Also, we must consider that in the upcoming surveys, such as LSST or Euclid, the data size will be too large to inspect visually. In this

scenario, relying solely on improved automated methods to purify the sample and accepting a small fraction of false positives could be a feasible solution.

## 6. The new sample of DES DR1 LSBGs

### 6.1. The newly identified LSBG sample

The optical color of a galaxy can give insights into its stellar population. Conventionally, based on their color, the galaxies are divided into red and blue galaxies, and it has been known that color is strongly correlated to the morphology of a galaxy (Strateva et al. 2001). Blue color galaxies are usually found to be highly active star-forming spiral or irregular systems. In contrast, red color galaxies are mostly found to be spheroidal or elliptical. In addition, the red galaxies have also been found to tend to cluster together compared to the blue galaxies (Bamford et al. 2009).

The LSBGs found by Tanoglidis et al. (2021b) have found a clear bimodality in the  $g - i$  color distribution similar to the LSBGs found by Greco et al. (2018). In the left panel of Fig. 11, we present the  $g - i$  color distribution of the 4 083 new LSBGs and the 23,790 LSBGs found by Tanoglidis et al. (2021b). We follow the criteria defined by Tanoglidis et al. (2021b) to define red galaxies as galaxies having  $g - i > 0.6$  and blue galaxies as galaxies having  $g - i < 0.6$  where  $g$  and  $i$  represent the magnitude in each band. In the right panel of Fig. 11, we present the color as a function of mean surface brightness in  $g$ -band for the new sample identified in this work and the LSBGs identified by Tanoglidis et al. (2021b). There are 1112 red LSBGs and 2,944 blue LSBGs in the new LSBG sample.<sup>4</sup> From Fig. 11, we can see that we have identified a relatively large fraction of blue LSBGs compared to Tanoglidis et al. (2021b) and a considerable fraction of new red LSBGs with  $g - i \geq 0.80$  and a mean surface brightness less than  $25.0 \text{ mag arcsec}^{-2}$ . The bias against blue LSBGs and highly red LSBGs in the sample created by Tanoglidis et al. (2021b) may have been caused by the bias in the training set used to create the SVM, which preselected the LSBG candidates. This bias could have occurred because a large fraction of their training set consisted of LSBGs near the Fornax cluster, which are mainly red LSBGs.

Looking at the distribution of  $\bar{\mu}_{eff}$  values of the new sample, both the red and blue LSBGs have a similar mean surface brightness range, with a median  $\bar{\mu}_{eff}$  of 24.75 and 24.68  $\text{mag arcsec}^{-2}$ , respectively. Both populations of red LSBGs and blue LSBGs from the new sample have sizes ranging from  $2.5'' - 20''$ . However, as mentioned earlier, most of these LSBGs have radii less than  $7''$ , with a median of  $4.01''$  for blue LSBGs and  $3.59''$  for red LSBGs. In comparison, blue LSBGs tend to have larger angular radii compared to red LSBGs. The Sérsic index distribution of the red and blue LSBGs in the new sample has similar distribution and almost equal median values (0.847 and 0.845 for red and blue LSBGs, respectively). A median Sérsic index of around 0.84 indicates that the majority of the galaxies are closer to a disk-shaped geometry, irrespective of their color. The distribution of the axis ratio of the red and blue LSBGs from the new sample shows a clear difference, as shown in Fig. 12. The median of the axis ratio distribution of the blue and red LSBGs is 0.7 and 0.8, respectively. This indicates that, in general, the red LSBGs are rounder than the blue LSBGs.

<sup>4</sup> 27 LSBGs failed the modelling using GalFit for  $i$ -band, and they are not included in this color analysis.

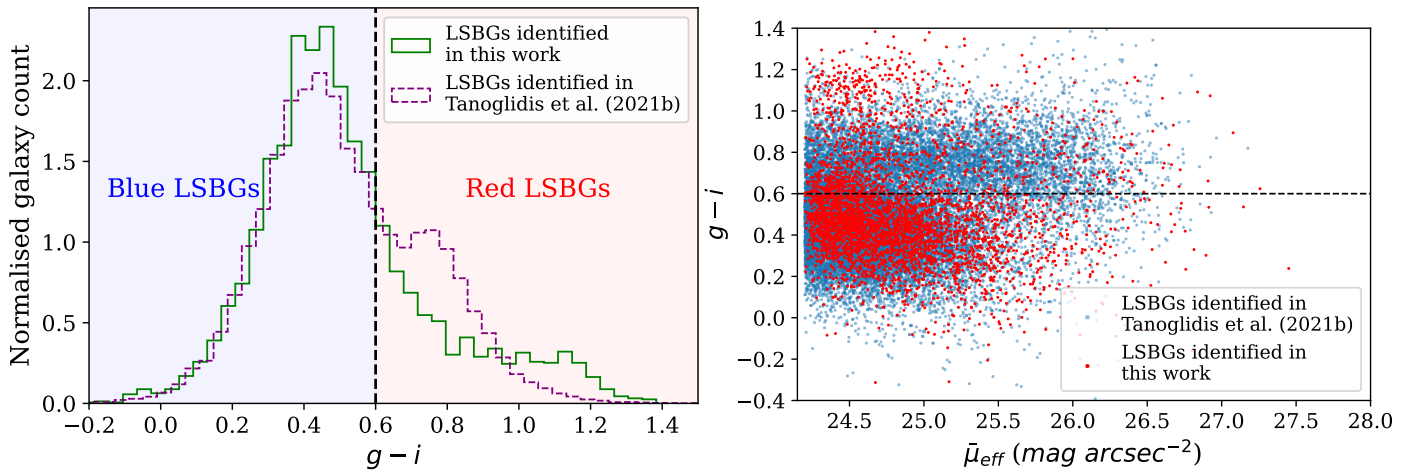


Fig. 11: Normalised distribution of color of the LSBGs from the new sample identified in this work and the LSBGs identified by Tanoglidis et al. (2021b) plotted in the left panel. The right panel shows the color as a function of mean surface brightness in the  $g$ -band for the new sample identified in this work and the LSBGs identified by Tanoglidis et al. (2021b). The dashed line shows the separation between red and blue LSBGs.

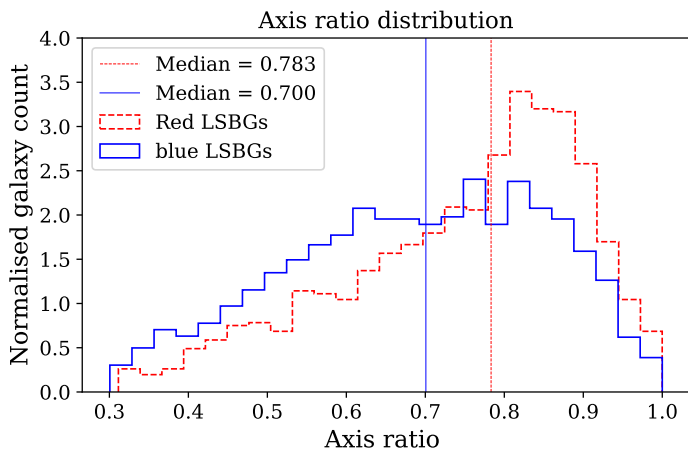


Fig. 12: Normalised distribution of axis ratio (left panel) of red and blue LSBGs from the new sample. The vertical lines show the median for each class.

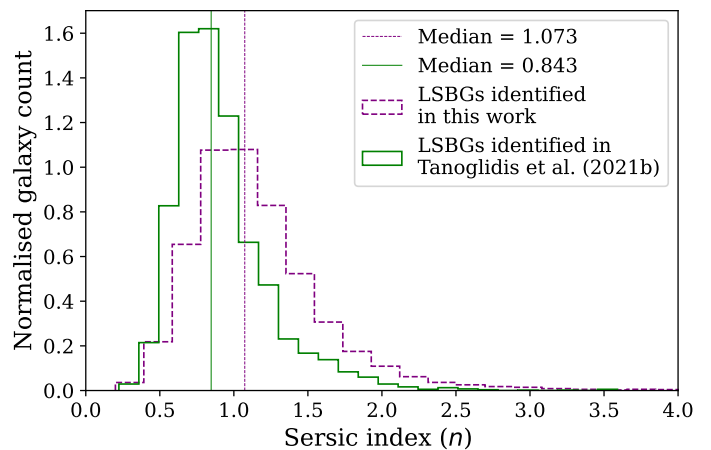


Fig. 13: Normalised distribution of the Sérsic index of the LSBGs identified in this work and by Tanoglidis et al. (2021b). The vertical lines show the median for each class

## 6.2. Why are there additional LSBGs?

One of the other things to investigate at this moment will be how different the new LSBG sample is compared to the LSBGs identified by Tanoglidis et al. (2021b). Or, more precisely, one could wonder why these many LSBGs have been missed previously and whether it is somehow related to the nature of these galaxies. Apart from the Sérsic index, all other Sérsic parameters of the new and the old sample have an almost similar distribution. The distribution of the Sérsic index for the new sample identified in this work and the LSBG sample identified by Tanoglidis et al. (2021b) is shown in Fig. 13. The new LSBG sample has a Sérsic index predominantly in the range  $n < 1$ , which is comparatively lower than the Sérsic index distribution of LSBGs identified by Tanoglidis et al. (2021b). However, this does not point to any reason why these LSBGs were missed in the previous search, and moreover, Tanoglidis et al. (2021b) have also commented on the under-representation of red LSBGs with small Sérsic index in their sample.

To answer the aforementioned question, a close inspection of the methodology of Tanoglidis et al. (2021b) shows that most of the new LSBGs (82%) we identified here were missed by the SVM in their first pre-selection step. This shows the importance of methodology in preselecting the samples. Since the methodology used by Tanoglidis et al. (2021b) and Greco et al. (2018) have considerable similarities (e.g., usage of SVM), this indicates that Greco et al. (2018) might have also missed some LSBGs from the HSC-SSP survey and the fraction should be greater in comparison to Tanoglidis et al. (2021b). It should be noted that there is a slight overlap in the regions of observation by Greco et al. (2018) and DES, as shown in Fig. 14. There are 198 LSBGs identified by Greco et al. (2018) from HSC-SSP in the field of view of DES and detected in the DES Y3 gold catalogue. Among these 198 LSBGs, Tanoglidis et al. (2021b) has recovered 183 LSBGs, and we recovered 10 more additional LSBGs from this field, making the total number of recovered LSBGs to 193. We would also like to point out that there are additional LSBGs ( $\sim 200$ ) in our total sample in the same region,

but missed by Greco et al. (2018), even though the HSC-SSP data used by Greco et al. (2018) is about 2 orders of magnitude deeper than the DES DR1. However, we have also missed some LSBGs ( $\sim 150$ ) that have been identified by Greco et al. (2018). These LSBGs were not detected in the DES Y3 gold catalogue and subsequently were missed by the searches by Tanoglidis et al. (2021b) and ours. With the DES data release 2 (DES DR 2) having an improved depth ( $\sim 0.5$  mag; Abbott et al. 2021), we should expect an increase in the number of LSBGs from DES. Therefore, there is a potential for using transfer learning with transformers in the future search for LSBGs from DES DR 2 (Abbott et al. 2021) and HSC-SSP data release 3 (Aihara et al. 2022).

With the addition of the new 4083 LSBGs, the number of LSBGs in the DES increased to 27,873, effectively increasing the average number density of LSBGs in DES to  $\sim 5.5$  deg $^{-2}$ . In addition, it should also be noted that there are still around  $\sim 3000$  candidates identified by the ensemble models, which have not undergone further analysis to be verified as LSBGs. Potentially indicating that the number of LSBGs in DES might increase further in future. Hence the average number density of  $5.5$  deg $^{-2}$  reported here can only be taken as a lower limit. Earlier, Greco et al. (2018) estimated that the average number density of LSBGs in HSC-SSP is  $\sim 3.9$  deg $^{-2}$ . However, this estimate was based on LSBG samples with  $\bar{\mu}_{eff} > 24.3$  mag arcsec $^{-2}$ , unlike the  $\bar{\mu}_{eff} > 24.2$  mag arcsec $^{-2}$  selection we adopted in this work. For a similar selection on  $\bar{\mu}_{eff} > 24.2$  mag arcsec $^{-2}$  in the combined sample presented here (LSBGs identified in this work + LSBGs identified by Tanoglidis et al. (2021b)), we obtain a higher number density of  $4.9$  deg $^{-2}$ , compared to the previous estimates ( $3.9$  deg $^{-2}$  from Greco et al. (2018) and  $4.5$  deg $^{-2}$  from Tanoglidis et al. (2021b)).

As discussed above, the number density of the LSBGs will be influenced by the methodology used to search for the LSBGs. Similarly, one other intrinsic factor that can influence the number density is the completeness of the survey. Improved imaging techniques can reveal fainter objects, leading to an increase in the number density. The completeness of a survey can be determined by plotting the galaxy number count, and one could also have a rough idea about the redshift distribution of the objects of interest by comparing it with the Euclidean number count. Fig. 15 shows the number count of LSBGs identified in DES (this work and Tanoglidis et al. (2021b)) and HSC (Greco et al. 2018). As expected, HSC has better completeness than DES. However, HSC still has a smaller number density than DES, which is evident from comparing the peaks of both number counts. The slope of the number counts near 0.6 (representing Euclidean geometry) for both HSC and DES suggest that most identified LSBGs are local (Yasuda et al. 2001). Furthermore, E Greene et al. (2022) has analysed the LSBG sample from HSC and estimated that the 781 LSBGs identified by Greco et al. (2018) have a redshift less than 0.15.

With the increasing number of LSBGs identified from different surveys, one of the other questions that need to be addressed at this moment is the definition of an LSBG itself. One could define a different definition for an LSBG, consequently leading to finding a completely different sample of LSBGs from the same dataset, which in turn can affect the conclusions of the study. One of the primary factors contributing to these discrepancies is the current reliance on surface brightness-based definitions for LSBGs, which are contingent upon the observation band in use. Different observation bands may involve distinct threshold values. Depending on the band we use, the LSBG definition will

likely vary. In this scenario, one potential solution is to define an LSBG based on the stellar mass density of the galaxy. Current definitions based on the stellar mass density define an LSBG as a galaxy with a stellar mass density,  $\Sigma_{star} \lesssim 10^7 M_{\odot} \text{ kpc}^{-2}$  (e.g., Carleton et al. 2023). Following Eq. 1 of Chamba et al. (2022), we made an estimate of the stellar mass surface density using our observed  $i$ -band surface brightness  $\bar{\mu}_{eff}$  and the stellar mass-to-light ratio obtained from the  $g - i$  color (Du et al. 2020). The stellar mass surface density distribution of the LSBGs from DES and HSC-SSP is shown in Fig. 16. Here we can see that most of the LSBGs satisfy this condition, and only a small percentage stay above the threshold of  $10^7 M_{\odot} \text{ kpc}^{-2}$ . On average, the LSBGs from DES have a higher stellar mass surface density than those from HSC-SSP, which could be attributed to the higher depth in the data used by Greco et al. (2018). However, as argued by Chamba et al. (2022), accurate estimation of the stellar mass density requires deep photometry in multiple bands. In our case, we employed a single color, and as a result, the constraints we derived on the stellar mass density may be limited in accuracy.

## 7. Clustering of LSBGs in DES

The on-sky distribution of the red and blue LSBGs identified in this work, along with those identified by Tanoglidis et al. (2021b), is shown in Fig. 17 and Fig. 18. In the local universe, "normal" high surface brightness red galaxies tend to cluster together, while blue galaxies are much more dispersed in the field (Zehavi et al. 2005). Such a trend is also clearly visible for the LSBG sample. As seen in Fig. 17, red LSBGs tend to form concentrated nodes. In contrast, the blue LSBGs are distributed much more homogeneously in the sky, as seen in Fig. 18.

A two-point auto-correlation function is a statistical tool commonly used to quantify the galaxy clustering (Peebles 1980). Here we use the angular two-point auto-correlation function,  $\omega(\theta)$ , computed using the Landy & Szalay (1993) estimator defined as

$$\omega = \frac{\hat{D}\hat{D}(\theta) - 2\hat{D}\hat{R}(\theta) + \hat{R}\hat{R}(\theta)}{\hat{R}\hat{R}(\theta)}, \quad (11)$$

where

$$\hat{D}\hat{D} = \frac{DD(\theta)}{n_d(n_d - 1)/2}, \quad (12)$$

$$\hat{D}\hat{R} = \frac{DR(\theta)}{n_d n_r}, \quad (13)$$

$$\hat{R}\hat{R} = \frac{RR(\theta)}{n_r(n_r - 1)/2}. \quad (14)$$

Here  $DD(\theta)$  is the number of pairs in the real sample with angular separation  $\theta$ ,  $RR(\theta)$  is the number of pairs within a random sample,  $DR(\theta)$  is the number of cross pairs between the real and random samples,  $n_d$  is the total number of real data points, and  $n_r$  is the total number of random points.

We use a random sample of 4491746 points generated from the DES footprint mask. To compute  $\omega(\theta)$  we employ `treecorr` (Jarvis 2015). Errors are estimated using jackknife resampling where the sky is divided into 100 equal-sized batches for resampling (Efron & Gong 1983). For high surface brightness galaxy samples, the angular correlation function very often can be well fitted by a single power-law (Peebles & Hauser 1974; Peebles 1980; Hewett 1982; Koo & Szalay 1984; Neuschaefer et al. 1991)

$$\omega(\theta) = A\theta^{1-\gamma} \quad (15)$$

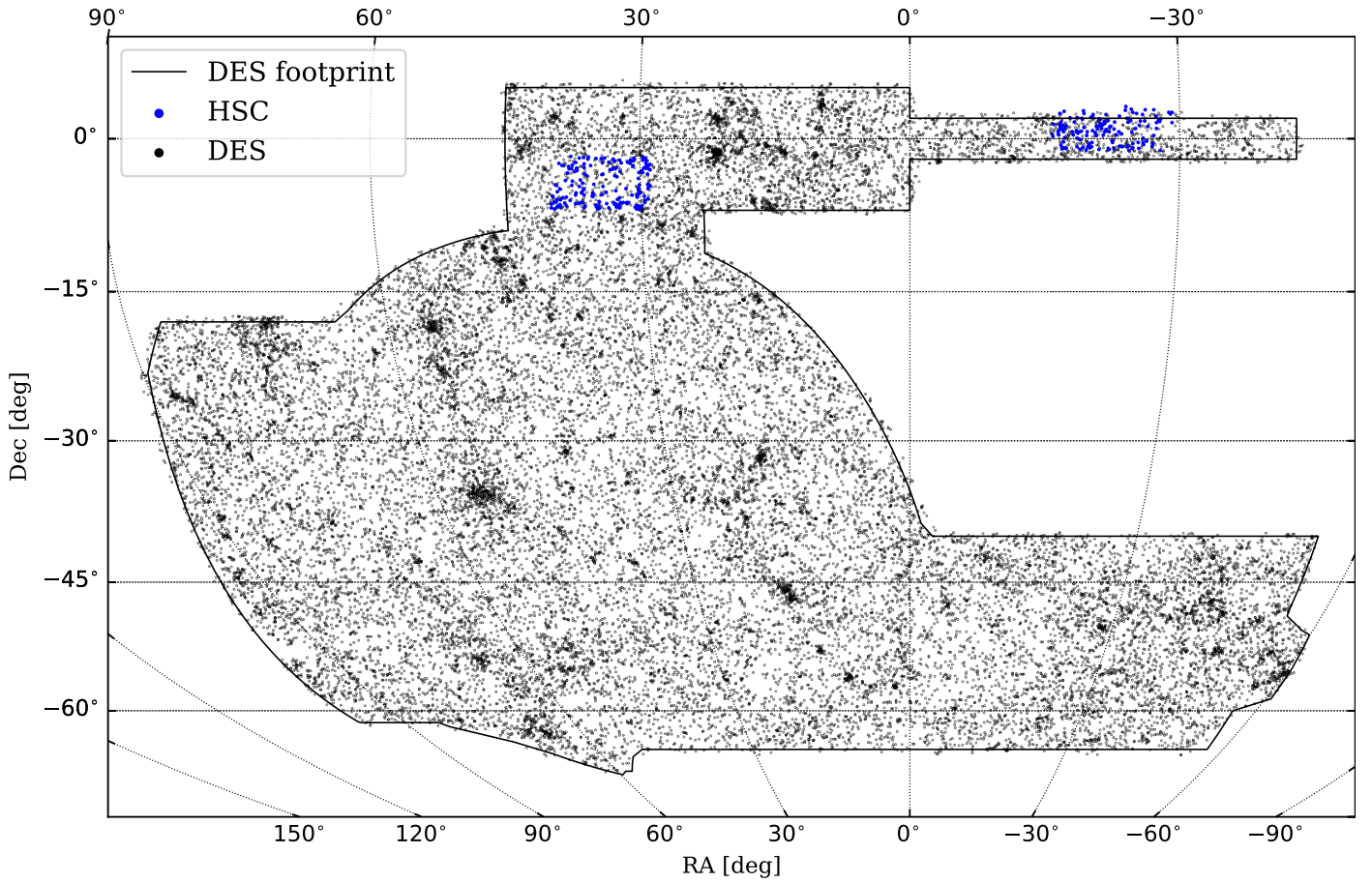


Fig. 14: Sky distribution of the LSBGs identified from DES (black dots) by [Tanoglidis et al. \(2021b\)](#) + this work and the LSBGs identified from HSC-SSP (blue dots) by [Greco et al. \(2018\)](#).

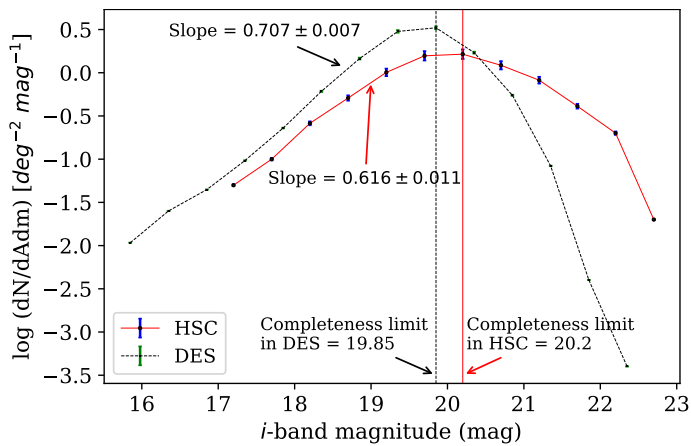


Fig. 15: The number count of galaxies as a function of  $i$ -band magnitude, with the y-axis displaying the logarithm of the number density per apparent magnitude. The red line with the blue error bars represents the data from HSC, and the black dashed line with green error bars represents the data from DES.

where  $A$  is the amplitude which represents the strength of the clustering, and  $\gamma$  represents the rate at which the strength of the

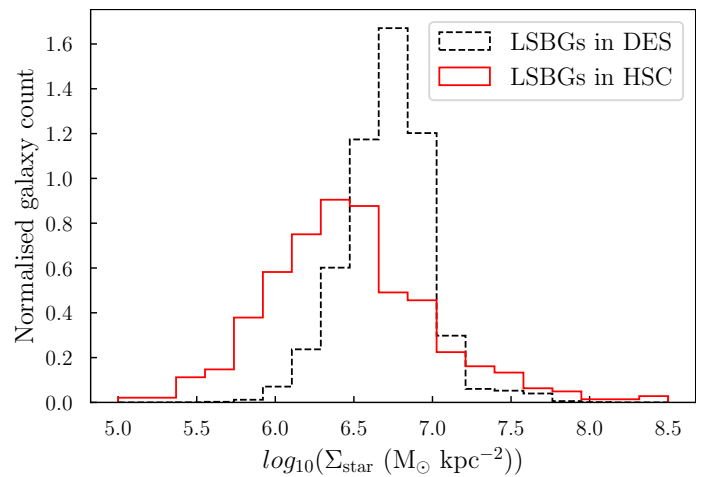


Fig. 16: Normalised distribution of stellar mass surface density of LSBGs identified in HSC (red line) and DES (black line).

clustering reduces as we go to large angular scales. This power-law behaviour is usually observed in a wide range of angular scales; however, it is not universal, especially on the smallest scales. Full modelling of the shape of the correlation function re-



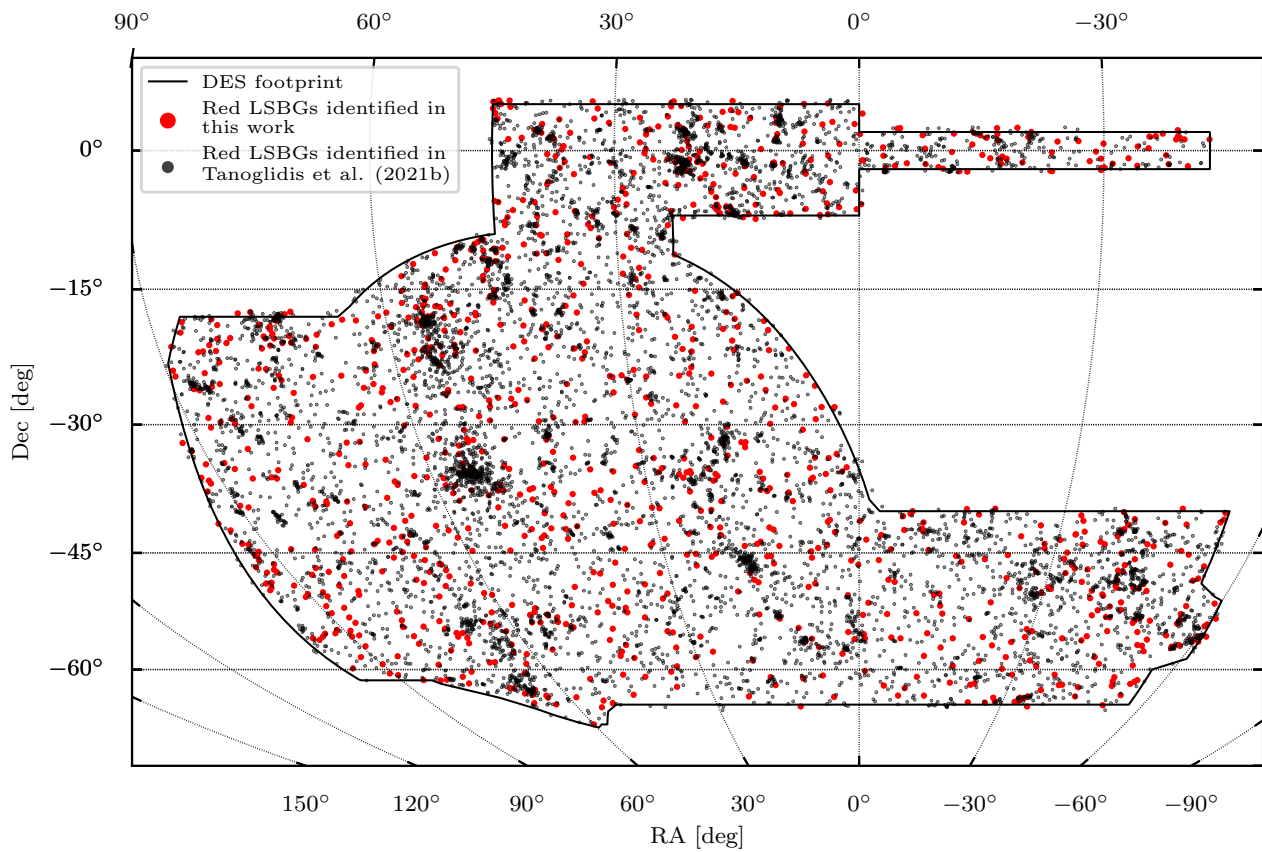


Fig. 17: Sky distribution of red LSBGs identified in this work (red dots) and the LSBGs identified (black dots) by [Tanoglidis et al. \(2021b\)](#).

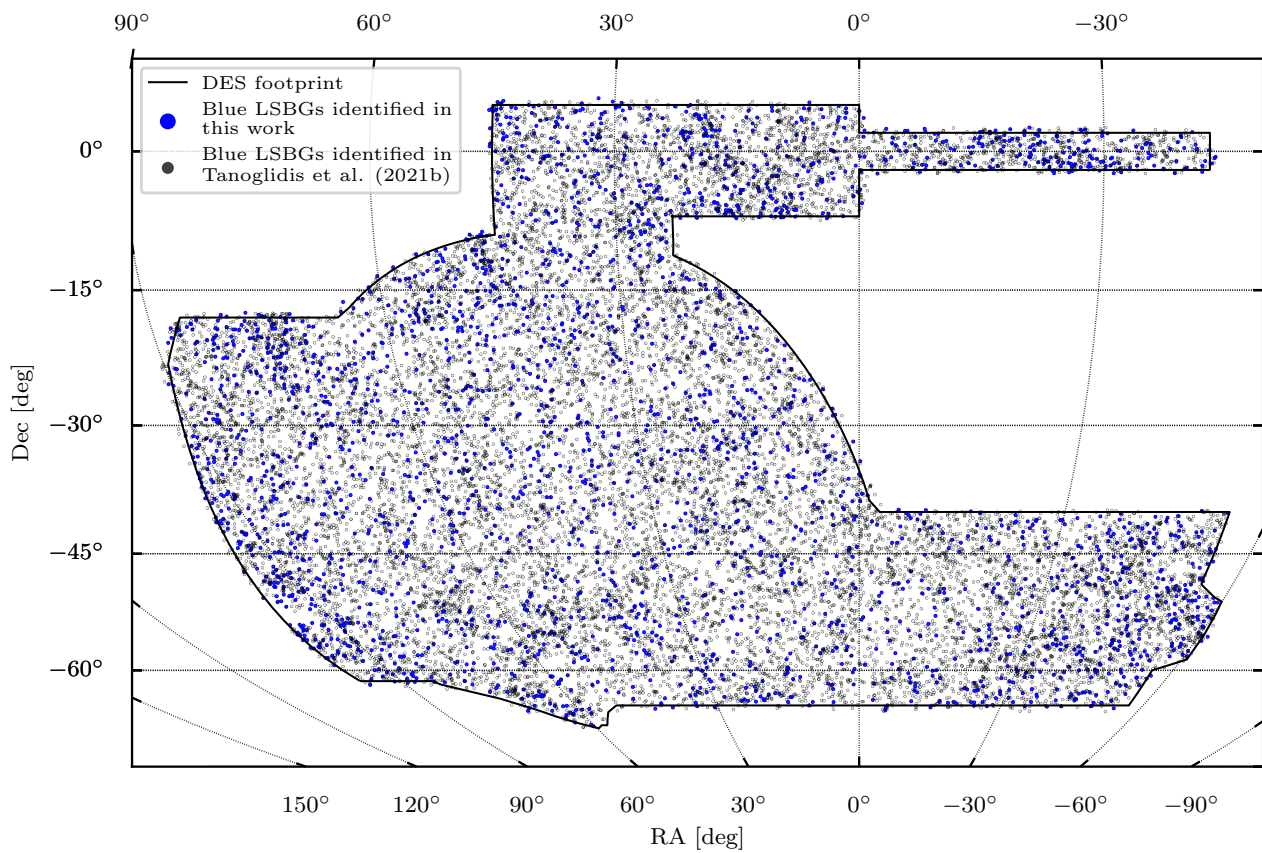


Fig. 18: Sky distribution of blue LSBGs identified from the new sample (blue dots) and the LSBGs identified (black dots) by [Tanoglidis et al. \(2021b\)](#).

quires taking into account different processes governing galaxy clustering on small scales (corresponding to galaxies located in the same dark matter halo) and at larger scales (corresponding to clustering of different haloes). This modelling is usually done using the halo occupation distribution models (HOD) (Ma & Fry 2000; Peacock & Smith 2000; Zheng et al. 2005; Kobayashi et al. 2022). In this work, however, we perform only a preliminary analysis and base interpretation of our data on the power-law fitting only.

To compare the clustering of the LSBGs with the clustering of the high surface brightness galaxies (HSBGs), we constructed a control sample of HSBGs from the DES data. For this purpose, we selected galaxies in the surface brightness range  $20.0 < \bar{\mu}_{eff} < 23$  mag arcsec<sup>-2</sup> and in the magnitude range  $17 < g < 23$  mag (which is the same magnitude range as our LSBG sample). Additionally, we applied a photometric redshift  $z < 0.1$  cut in order to keep the HSBGs sample consistent with the LSBGs, which are also expected to be mostly local (E Greene et al. 2022). For this purpose, we used the photometric redshifts from the DES Y3 gold catalogue calculated using the Directional Neighbourhood Fitting (DNF) algorithm (Sevilla-Noarbe et al. 2021; De Vicente et al. 2016). In addition, we also applied the selection cuts on the parameters from SourceExtractor such as SPREAD\_MODEL, EXTENDED\_CLASS\_COADD and on colors (using the MAG\_AUTO magnitudes) as described in Sect. 2.2.

Initially, we computed the angular two-point auto-correlation function for the samples of LSBGs and HSBGs. Then we split the samples into red and blue galaxies to measure their clustering properties separately. For LSBGs, we followed the criterion defined in Sect. 6, i.e. a color cut of  $g - i = 0.6$  mag to separate blue and red sources. As seen from the color histogram presented in Fig. 19, the HSBGs show a bi-modality around  $g - i = 1.0$  mag, which can be most likely attributed to their different stellar masses. Consequently, we use the boundary  $g - i = 1.0$  mag to divide our HSBG sample into red and blue sub-samples. The properties of all the samples used for the measurement of the galaxy clustering, together with the best-fit power-law parameters, are listed in Table 4. The 2-point auto-correlation functions for all the samples described above are shown in Fig. 20.

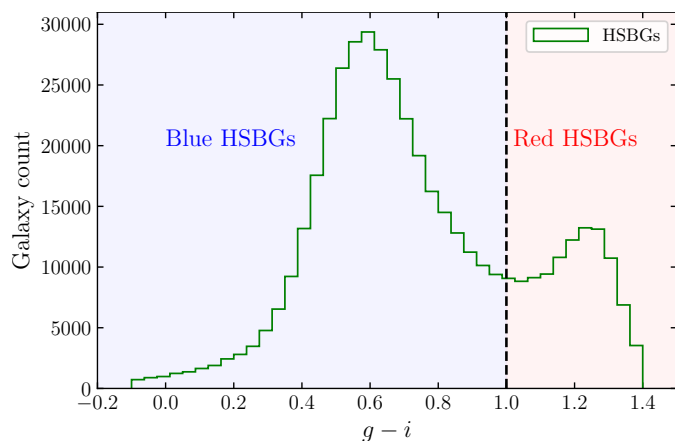


Fig. 19: Color distribution of the HSBGs from the DES DR1. The vertical line at  $g - i = 1.0$  shows the color separation of the HSBGs into red and blue galaxies.

As it is clear from Fig. 20, the angular two-point auto-correlation function of the red LSBGs does not follow a power law at small angular scales. Therefore, the power-law fits were only performed in the range of 0.15 deg to 7 deg to avoid them

Table 4: Best-fitting power law parameters for the angular two-point auto-correlation function for HSBG and LSBGs along with the information on the number of galaxies, median  $g$ -band magnitude, and the mean surface brightness for each sample.

Sample	Number of galaxies	Median $g$ (mag)	Median $\bar{\mu}_{eff}$ (mag arcsec <sup>-2</sup> )	$A$	$\gamma$
All HSBGs	451,310	18.84	21.66	0.091 ±0.004	1.651 ±0.021
Red HSBGs	103,900	17.96	21.21	<b>0.245 ±0.004</b>	<b>1.848 ±0.012</b>
Blue HSBGs	347,410	19.21	21.81	0.0648 ±0.004	1.631 ±0.036
All LSBGs	27,840	20.11	24.66	0.138 ±0.013	1.941 ±0.048
Red LSBGs	18,924	20.23	24.89	<b>0.671 ±0.079</b>	<b>2.090 ±0.071</b>
Blue LSBGs	8,916	20.07	24.59	0.051 ±0.001	1.620 ±0.025

being affected by the one-halo effects. In part well fitted by the power law, for the red LSBGs,  $\omega(\theta)$  is significantly steeper than for the blue LSBGs. However, it flattens at smaller scales, i.e. between 0.01 deg and 0.2 deg; this behaviour is also transmitted to the full sample of LSBGs. In contrast, the blue LSBGs follow a power law behaviour, with a lower clustering amplitude and a much less steep slope, in almost all the angular scales. This behaviour of the angular correlation function might be explained by the observations by van der Burg et al. (2016) and Wittmann et al. (2017) that the number of LSBGs close to the cores of galaxy clusters decreases. Such suppression may reduce the clustering power on small scales, leading to a flattening in the auto-correlation function, which is seen for the red LSBGs, which are mostly associated with clusters.

Comparison of clustering of the LSBGs and the HSBGs also shows notable differences. Not surprisingly, red samples, both of HSBGs and LSBGs, are more clustered than their blue counterparts. At the same time, the red LSBG sample has a significantly higher clustering amplitude than the reference red HSBG sample. Red LSBGs also display a steeper slope of  $\omega(\theta)$  at angular scales larger than 0.15 deg, but at smaller scales, their  $\omega(\theta)$  flattens, unlike in the case of red HSBGs for which we can even observe a hint of an upturn which can be associated with a one-halo term. This picture is consistent with a scenario in which red LSBGs are mostly associated with dense structures like clusters but do not populate their centres but rather the outskirts. In contrast, red HSBGs display the usual behaviour of red passive galaxies, appearing in a variety of environments, with a tendency to cluster and gather most strongly in the cluster centres.

Blue LSBGs have a significantly lower clustering amplitude than their HSBG counterparts. At the same time, the slope of their  $\omega(\theta)$  at scales larger than 0.15 deg remains very similar. The blue HSBGs and LSBGs follow the usual distribution of blue star-forming galaxies, dispersed in the field and avoiding clusters. These results are consistent with the results obtained by Tanoglidis et al. (2021b) for their sample of DES LSBGs. They compared the clustering of LSBGs with very bright galaxies in the magnitude range of  $14 < g < 18.5$  mag from the 2MPZ cat-

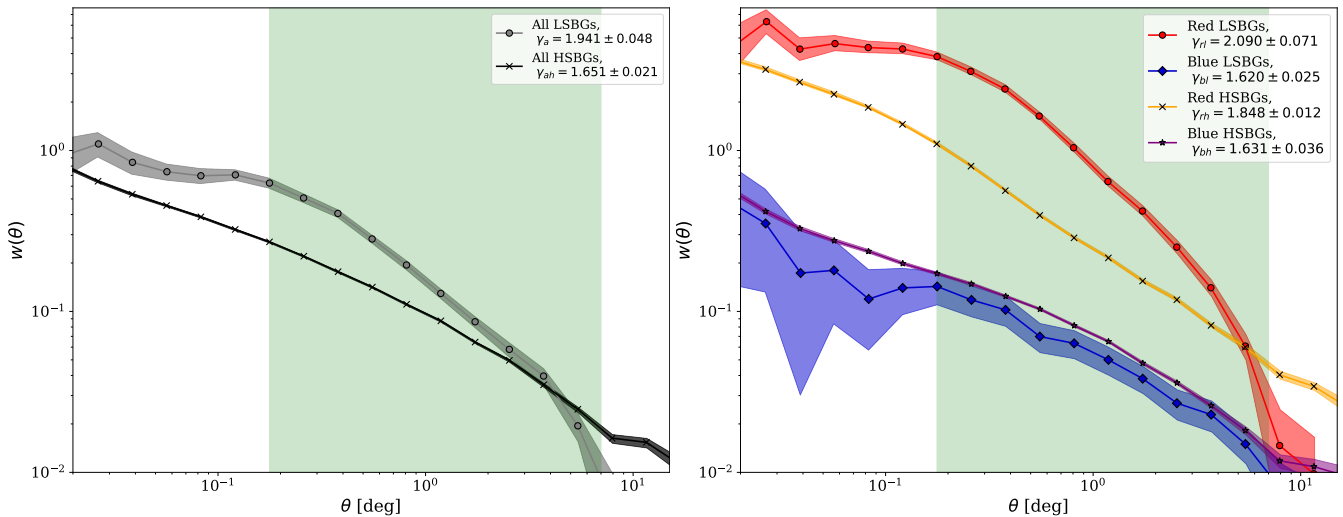


Fig. 20: Angular autocorrelation function for the full sample of LSBGs (grey line with open circles) and the sample of HSBGs (black line with crosses) is shown in the left panel. The angular autocorrelation function of the red LSBGs (red line), blue LSBGs (blue line), red HSBGs (orange line) and blue HSBGs (purple line) is shown in the right panel. The vertical green shaded region represents the region fitted for a power law ( $\omega = A\theta^{1-\gamma}$ ), and the corresponding  $\gamma$  values are shown in the legend.

alogue (Bilicki et al. 2014). They found that LSBGs had higher clustering amplitude in the range of 0.1 to 2 degrees, which is similar to our observations.

However, our results contradict the early estimates from Bothun et al. (1993) and Mo et al. (1994), who infer that the LSBGs tend to cluster weakly spatially. However, their analyses were limited by a small data sample ( $\sim 400$  LSBGs), a small area of the sky, and most likely selection biases. Given the low accuracy of photometric redshifts for LSBGs in our sample, we do not attempt to reconstruct their spatial clustering in this work. Further analysis is planned as a follow-up to this study.

## 8. Identification of ultra-diffuse galaxies

As discussed in Sect. 1, UDGs are a subclass of LSBGs that have extended half-light radii  $r_{1/2} \geq 1.5$  kpc and a central surface brightness  $\mu_0 > 24$  mag arcsec $^{-2}$  in  $g$ -band (van Dokkum et al. 2015). Significant population of UDGs have been discovered in the Coma cluster by van Dokkum et al. (2015) and other investigations have revealed a large number of UDGs in other galaxy clusters (Koda et al. 2015; Mihos et al. 2015; Lim et al. 2020; La Marca et al. 2022a,b). Later on, studies have shown that thousands of UDGs can be found in single individual clusters and that the abundance of UDGs scales close to linearly with host halo mass (van der Burg et al. 2016; Mancera Piña et al. 2018).

In order to investigate if there are any cluster UDGs in the sample of LSBGs we identified in DES, we crossmatched our total LSBG sample (23,790 LSBGs from Tanoglidis et al. 2021b and the 4083 new LSBGs we identified) with the X-ray-selected galaxy cluster catalogue from the ROSAT All-Sky Survey (RXGCC; Xu et al. 2022). All the LSBGs at the angular distance from the centre of the cluster lower than  $R_{200}^5$  virial radius of the cluster were associated with that cluster. Here,  $R_{200}$

<sup>5</sup> We used the  $R_{500}$  values and the redshifts provided by Xu et al. (2022) to obtain the  $R_{200}$  crossmatching radius. Following Ettori & Balestra (2009), we assume  $R_{200} \approx R_{500}/0.65$  where  $R_{500}$  is the radius at which the average density of a galaxy cluster is 500 times the critical density of the universe at that redshift.

is the radius at which the average density of a galaxy cluster is 200 times the critical density of the universe at that redshift. We found that 1310 LSBGs from the combined catalogue and 123 LSBGs from our new sample were associated with 130 and 53 clusters, respectively. Using the redshift of the cluster provided in Xu et al. (2022), and assuming that the associated LSBG is at the same redshift as the cluster, we estimated the half-light radius of the LSBG and its projected comoving distance from the cluster centre. It should be noted that since we perform our crossmatching with only projected distances, some of the LSBGs associated with clusters could be non-cluster members that are projected along the field. However, it is unlikely to be the case for all, and since we do not have any other distance estimate for the LSBGs, we chose to adopt this method. However, it should be also noted that UDGs are not exclusively located in clusters; they can also be observed in groups (Cohen et al. 2018; Marleau et al. 2021) and even in field environments (Prole et al. 2019). In this section, we are only focusing on the LSBGs and UDGs associated with the clusters.

Among the 1,310 cluster LSBGs, we further classify 317 cluster UDG candidates based on their half-light radius ( $r_{1/2} \geq 1.5$  kpc) and the central surface brightness ( $\mu_0 > 24.0$  mag arcsec $^{-2}$ ) in the  $g$ -band. Since we have not confirmed the physical distances to these galaxies and hence their physical sizes, they can only be regarded as UDG candidates. From here on-ward, when referring to UDGs in the paper, it is important to note that we are addressing UDG candidates and not confirmed UDGs. These 317 UDGs are distributed within 80 clusters making it the largest sample of clusters in which UDGs are studied. It should also be noted that Tanoglidis et al. (2021b) also identified 41 UDGs from their LSBG sample in DES by associating the 9 most overdense regions of LSBGs with known clusters. However, they did not study the properties of those 41 UDGs in detail, and the 276 UDGs among the 317 UDGs reported here are completely new. The UDGs presented here have a median  $r_{1/2}$  of 2.75 kpc and  $\mu_0$  of 24.51 mag arcsec $^{-2}$ . Six of the newly identified UDGs are shown in Fig. 21.

As seen from Fig. 22, the majority of the cluster UDGs (253 out of 317) are red in color ( $g - i > 0.6$  mag), which is similar

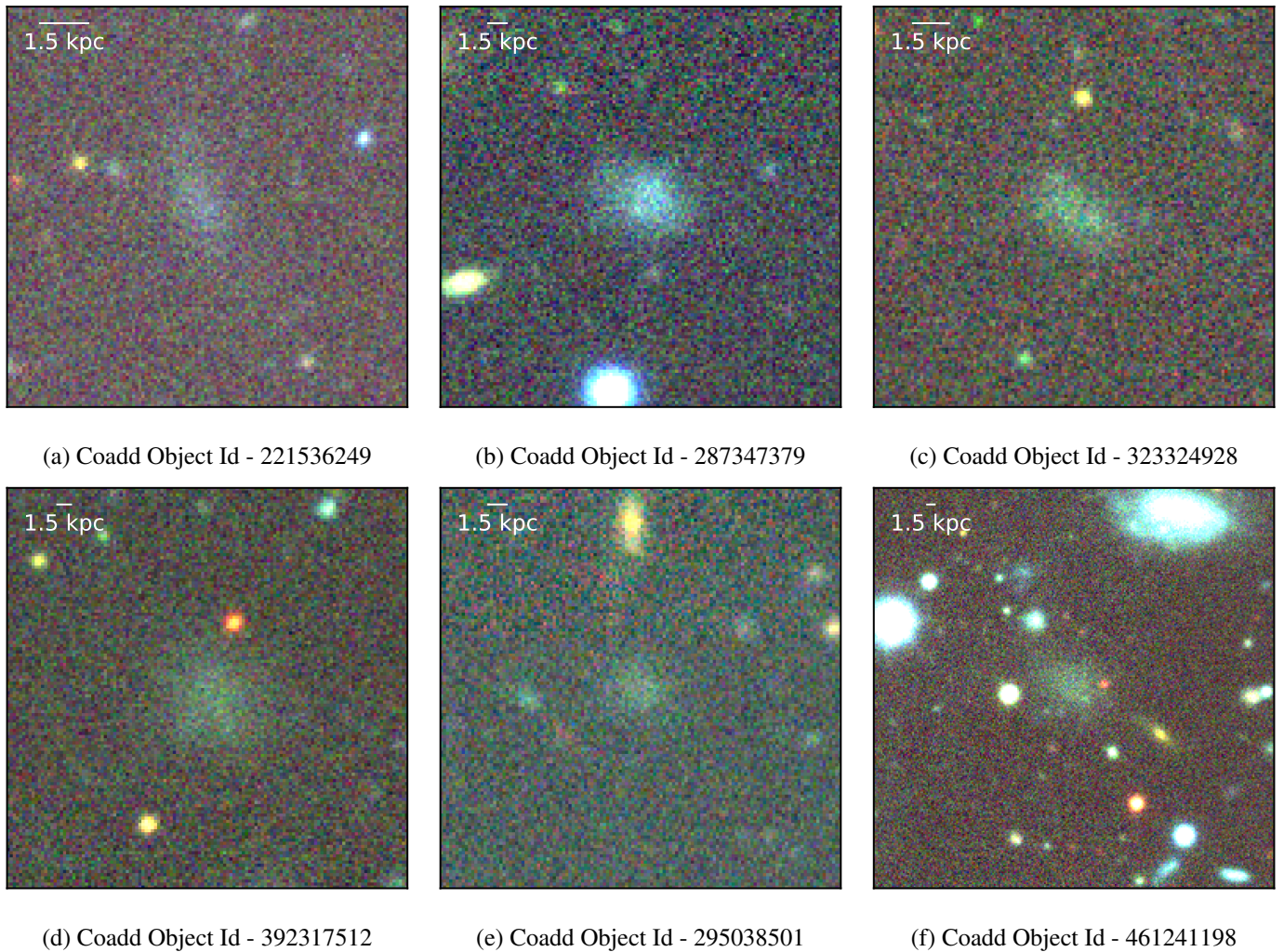


Fig. 21: Cutouts of 6 confirmed new UDGs. The unique identification number (co object id) for each galaxy in DES DR1 is given below each image. The images were generated by combining the  $g$ ,  $r$  and  $z$  bands using APLpy package (Robitaille & Bressert 2012), and each image corresponds to a  $33.66'' \times 33.66''$  region of the sky with the UDG at its centre.

to the trend of cluster LSBGs (909 out of 1310). This is consistent with theoretical predictions for cluster UDGs (Benavides et al. 2023). Mancera Piña et al. (2019) have also found similar distribution for the  $g - r$  color of 442 UDGs observed in 8 galaxy clusters. The joint distribution of the red and blues UDGs in the space of  $r_{1/2}$  and  $\mu_0$  is shown in Fig. 23. The red UDGs presented here have a median  $r_{1/2}$  of 2.75 kpc and  $\mu_0$  of 24.52 mag arcsec $^{-2}$ . Similarly, the blue UDGs have a median  $r_{1/2}$  of 2.78 kpc and  $\mu_0$  of 24.41 mag arcsec $^{-2}$ . Most of the red and blue UDGs have a half-light radius in the range  $1.5 < r_{1/2} < 6$  kpc. However, there is a small fraction of UDGs (6 out of 317) with  $r_{1/2} > 10$  kpc, which is all red and have  $\mu_0 < 25.0$  mag arcsec $^{-2}$  which might be good potential candidates for the follow-up studies.

For all the cluster LSBGs, we can see a gradient in color as shown in Fig. 24, where LSBGs towards the outskirts of clusters tend to be bluer than those in the centre. This is similar to the behaviour found in Virgo cluster LSBGs from Junais et al. (2022). However, for the cluster UDGs presented in this study, the color gradient appears much weaker, almost showing a flat distribution in comparison to the LSBGs. A similar weak trend, where more blue UDGs are found towards the cluster centre, was also noted by Mancera Piña et al. (2019). On the other hand, Román & Tru-

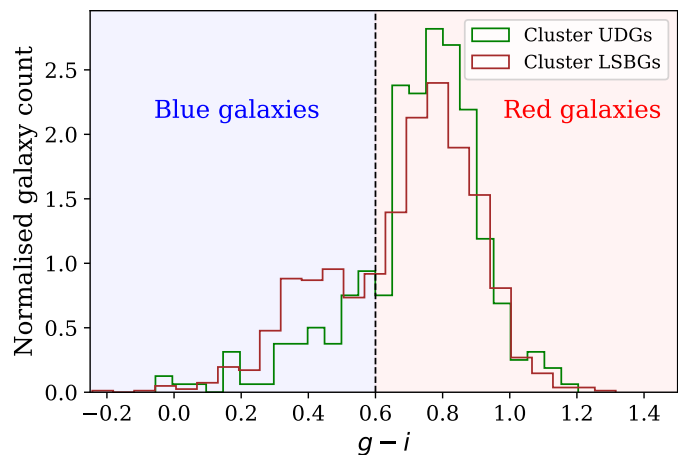


Fig. 22: Color distribution of the 1,310 cluster LSBGs and 317 cluster UDGs from the DES DR1.

jillo (2017) and Alabi et al. (2020) reported a more pronounced color trend as a function of cluster-centric distance, while La Marca et al. (2022b) did not find any significant trend. How-

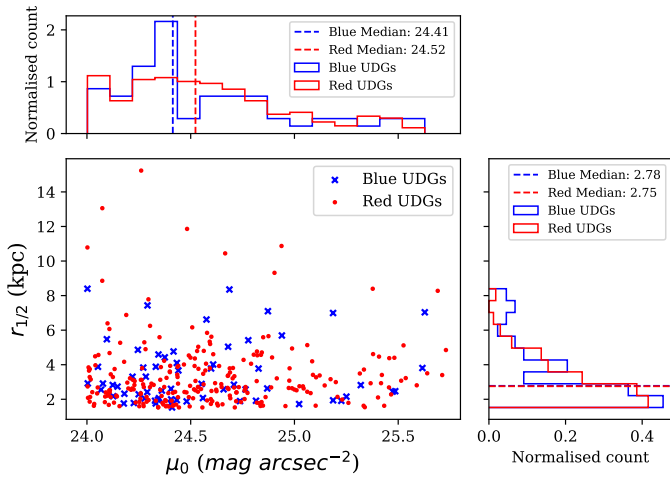


Fig. 23: Joint distribution of the red (red dots) and blue (blue cross) UDGs in the space of  $r_{1/2}$  and  $\mu_0$  in the  $g$ -band. The vertical lines in the histogram on the x-axis and y-axis show the median for each class.

ever, when directly comparing the trends in the color of UDGs in the cluster, one should keep in mind that these trends will be affected by several factors like the used bands for the color, sample size and the studied cluster, as we can see from the results in the literature. For example, our sample size ( $>300$ ) is similar to the sample size of Mancera Piña et al. (2019) and have similar results whereas it is different from the findings of Román & Trujillo (2017); Alabi et al. (2020) and La Marca et al. (2022b) which have a smaller sample size ( $<40$ ).

The trend observed in the half-light radius (Fig. 24) for both the cluster LSBGs and UDGs is quite evident. As we move towards the outer regions of the cluster centre, both LSBGs and UDGs show an increase in size. This behaviour is in agreement with the findings of Román & Trujillo (2017). The gradients we observe in color and size with respect to the cluster-centric distance are consistent with the proposed UDG formation scenarios such as the galaxy harassment (Conselice 2018), tidal interactions Mancera Piña et al. (2019), and ram-pressure stripping (Conselice et al. 2003b; Buyle et al. 2005). Such trends are also similar to what is observed for dwarf galaxies in the literature (Venholá et al. 2019), providing further support for the argument that UDGs can be considered as a subset of dwarf galaxies (Conselice 2018; Benavides et al. 2023).

The sample of UDG candidates presented here will be the subject of the follow-up analysis. Additionally, it should be noted that all the UDGs reported here are cluster UDGs. The actual number of UDGs in the LSBG catalogue (including low-density environments) might be more than this, and thus the reported number is only a lower limit on the total number of UDGs.

## 9. Conclusions

In this paper, we explore the possibilities of using transformers in distinguishing LSBGs from artefacts in optical imaging data. We implemented four transformer models that combined the use of CNN backbone and self-attention layers to classify the labels; we call them LSBG DETR (LSBG detection transformers) models. Similarly, we have created four transformer models that directly apply attention to the patches of the images without any convolutions and these models we call LSBG vision transformers. We

compared the performance of these two different architectures to the LSBG identification CNN model called DeepShadows presented in Tanoglidis et al. (2021a). We found that the transformer models performed better than the DeepShadows, and later we used the ensemble of our transformer models to look for new LSBGs in the DES DR1 data that the previous searches may have missed. We follow the definition of an LSBG used by Tanoglidis et al. (2021b), i.e. we define LSBGs as galaxies having a  $g$ -band mean surface brightness  $\bar{\mu}_{eff} > 24.2$  mag arcsec $^{-2}$  and half-light radii  $r_{1/2} > 2.5''$ . Following this definition, we identified 4 083 new LSBGs from the DES DR1, increasing the number of identified LSBGs in DES by 17%.

Our sample selection and LSBG identification pipeline consist of the following steps:

1. We preselect the objects from the DES Y3 Gold catalog based on the selection criteria described in Tanoglidis et al. (2021b) using the SourceExtractor parameters.
2. We applied the ensemble of transformer models to this sample of preselected objects. We chose the objects identified independently by both the LSBG DETR ensemble and the LSBG ViT ensemble for a further follow-up to be inspected for being an LSBG.
3. We performed a Sérsic fitting using Galfit and re-applied the selection cuts to further reduce the number of false positives. After this step, 4879 LSBG candidates remained to be visually inspected.
4. After the visual inspection, we report the presence of 4083 new LSBGs identified by the transformer ensemble models.

Following Tanoglidis et al. (2021b), we divided the total LSBG sample into two subsamples according to their  $g-i$  color. Among the 4083 new LSBGs presented here, 72% were identified as blue LSBGs, which is higher than the 67% observed in the sample presented by Tanoglidis et al. (2021b). Additionally, we also found that we have a more fraction of red LSBGs with color,  $g-i > 0.8$ , compared to the sample of LSBGs presented by Tanoglidis et al. (2021b). We speculate that the bias might have originated from the training set used by Tanoglidis et al. (2021b) to train the SVM model to preselect the LSBG candidate sample.

By combining the previously identified 23,790 LSBGs from Tanoglidis et al. (2021b) with the LSBGs newly identified in our work, the total number of known LSBGs in the DES is increased to 27,873. This increases the number density of LSBGs in the DES from 4.13 to 4.91 deg $^{-2}$  for LSBGs with  $\bar{\mu}_{eff} > 24.3$  mag arcsec $^{-2}$  and from 4.75 to 5.57 deg $^{-2}$  for LSBGs with  $\bar{\mu}_{eff} > 24.2$  mag arcsec $^{-2}$ . It should be stressed that this is a lower limit to the number density, and it would increase in the future with better imaging quality and better methodology for the surveys like LSST and Euclid.

We also made an analysis of the clustering of LSBGs in DES. We found that the LSBGs tend to cluster strongly in comparison to the HSBGs from DES, which is similar to the findings by Tanoglidis et al. (2021b). Upon further examination, we observed that the strong clustering tendency observed among low surface brightness galaxies (LSBGs) primarily stems from the red LSBGs, while the behaviour of blue LSBGs resembles that of blue high surface brightness galaxies (HSBGs) with weaker clustering tendencies. Additionally, we noted a decrease in the number of red LSBGs near the centre of the galaxy cluster, resulting in a flattening of the auto-correlation function on smaller scales which is similar to the conclusions of Wittmann et al. (2017).

Additionally, we crossmatched the LSBGs with the X-ray-selected galaxy cluster catalogue from the ROSAT All-Sky Sur-

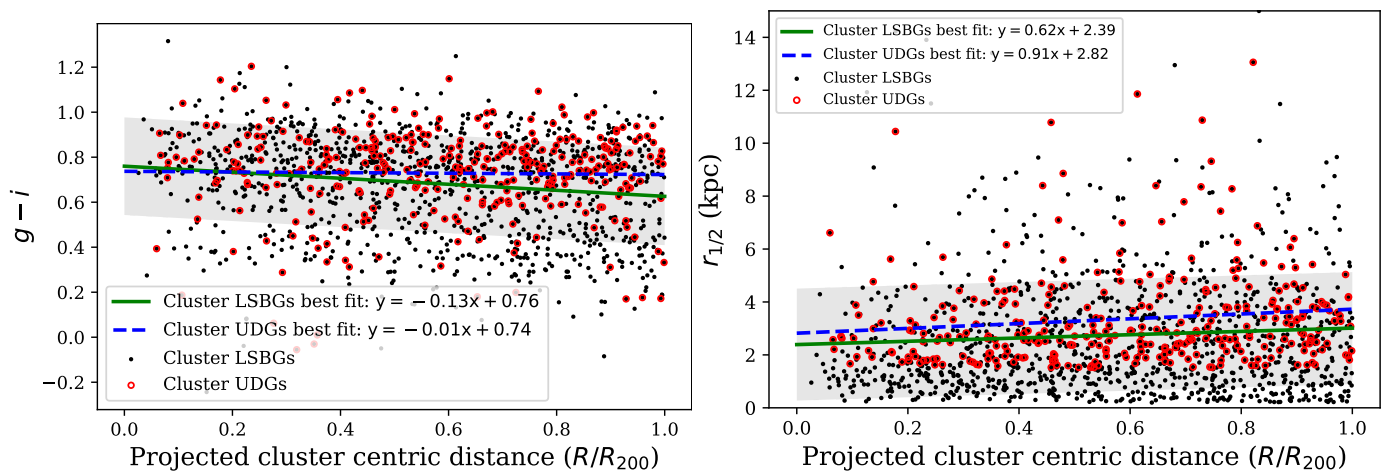


Fig. 24:  $g - i$  colour of the cluster LSBGs (black points) and  $r_{1/2}$  as a function of the projected distance from their cluster centre (in units of the cluster radius  $R_{200}$ ) is shown in the left and right panel respectively. The UDGs are marked as red hollow circles. The green line and the grey-shaded region are the linear best fit and the  $1\sigma$  scatter for the cluster LSBGs, respectively. The blue dashed line is the linear best fit for the cluster UDGs.

vey (RXGCC; Xu et al. 2022) to find LSBGs associated with the clusters. Using the redshift information of the clusters, we identify 317 UDGs, among which 276 are reported for the first time. We also observed a color gradient among the cluster LSBGs, where LSBGs located towards the outskirts of clusters exhibit a bluer color compared to those at the centre, similar to findings by Junais et al. (2022) in the Virgo cluster LSBGs. However, this trend is relatively weak for the cluster UDGs in our study, unlike the LSBGs. A clear trend in the half-light radius of the cluster LSBGs and UDGs as a function of the cluster-centric distance is also visible. The LSBGs and UDGs grow in size as going from the cluster centre to the outskirts. The coherent trends in the color and size are in agreement with the proposed UDG formation mechanisms such as the galaxy harassment (Conselice 2018), tidal interactions Mancera Piña et al. (2019), and ram-pressure stripping (Conselice et al. 2003b; Buyle et al. 2005), giving more support to the argument that the UDGs are a subset of dwarf galaxies (Conselice 2018; Benavides et al. 2023).

The upcoming large-scale surveys such as LSST and Euclid are expected to cover around 18 000 and 14 5000  $\text{deg}^2$  of the sky, respectively (Ivezić et al. 2019; Euclid Collaboration et al. 2022). Extrapolating our results on the number density of LSBGs, we are expected to find more than 100 000 and 80 000 LSBGs from LSST and Euclid, respectively. In this scenario, an improved and efficient methodology will be highly significant, and we propose that transformer models could overcome this difficulty. With the aid of transfer learning, we are planning to extend our study to HSC SSP DR3 and thus pave a pathway for the LSBG detection in LSST and Euclid.

*Acknowledgements.* J and KM are grateful for support from the Polish National Science Centre via grant UMO-2018/30/E/ST9/00082. US acknowledges support from the National Research Foundation of South Africa (grant no. 137975). This research was partially supported by the Polish National Science Centre grant UMO-2018/30/M/ST9/00757 and the Polish Ministry of Science and Higher Education grant DIR/WK/2018/12.

## References

Abbott, T. M. C., Abdalla, F. B., Allam, S., et al. 2018, *ApJS*, 239, 18  
 Abbott, T. M. C., Adamów, M., Aguena, M., et al. 2021, *ApJS*, 255, 20  
 Aihara, H., Aisayad, Y., Ando, M., et al. 2022, *PASJ*, 74, 247

Alabi, A. B., Romanowsky, A. J., Forbes, D. A., Brodie, J. P., & Okabe, N. 2020, *MNRAS*, 496, 3182  
 Allam, Tarek, J. & McEwen, J. D. 2021, arXiv e-prints, arXiv:2105.06178  
 Amorisco, N. C. & Loeb, A. 2016, *MNRAS*, 459, L51  
 Bamford, S. P., Nichol, R. C., Baldry, I. K., et al. 2009, *MNRAS*, 393, 1324  
 Benavides, J. A., Sales, L. V., Abadi, M. G., et al. 2023, *MNRAS*, 522, 1033  
 Bernstein, G. M., Nichol, R. C., Tyson, J. A., Ulmer, M. P., & Wittman, D. 1995, *AJ*, 110, 1507  
 Bertin, E. & Arnouts, S. 1996, *A&AS*, 117, 393  
 Bilicki, M., Jarrett, T. H., Peacock, J. A., Cluver, M. E., & Steward, L. 2014, *ApJS*, 210, 9  
 Bothun, G., Impey, C., & McGaugh, S. 1997, *PASP*, 109, 745  
 Bothun, G. D., Impey, C. D., Malin, D. F., & Mould, J. R. 1987, *AJ*, 94, 23  
 Bothun, G. D., Schombert, J. M., Impey, C. D., Sprayberry, D., & McGaugh, S. S. 1993, *AJ*, 106, 530  
 Burkholder, V., Impey, C., & Sprayberry, D. 2001, *AJ*, 122, 2318  
 Buyle, P., De Rijcke, S., Michielsen, D., Baes, M., & Dejonghe, H. 2005, *Monthly Notices of the Royal Astronomical Society*, 360, 853  
 Cabrera-Vives, G., Reyes, I., Förster, F., Estévez, P. A., & Maureira, J.-C. 2017, *ApJ*, 836, 97  
 Carion, N., Massa, F., Synnaeve, G., et al. 2020, in *Computer Vision – ECCV 2020*, ed. A. Vedaldi, H. Bischof, T. Brox, & J.-M. Frahm (Cham: Springer International Publishing), 213–229  
 Carleton, T., Cohen, S. H., Frye, B. L., et al. 2023, *ApJ*, 953, 83  
 Chamba, N., Trujillo, I., & Knapen, J. H. 2022, *A&A*, 667, A87  
 Chen, P.-C., Tsai, H., Bhojanapalli, S., et al. 2021, in *Proceedings of the 2021 Conference on Empirical Methods in Natural Language Processing (Online and Punta Cana, Dominican Republic: Association for Computational Linguistics)*, 2974–2988  
 Chen, Z., Duan, Y., Wang, W., et al. 2023, in *The Eleventh International Conference on Learning Representations*  
 Clevert, D., Unterthiner, T., & Hochreiter, S. 2016, in *4th International Conference on Learning Representations, ICLR 2016, San Juan, Puerto Rico, May 2-4, 2016, Conference Track Proceedings*, ed. Y. Bengio & Y. LeCun  
 Cohen, Y., van Dokkum, P., Danieli, S., et al. 2018, *ApJ*, 96  
 Conselice, C. J. 2018, *Research Notes of the American Astronomical Society*, 2, 43  
 Conselice, C. J., Gallagher, John S., I., & Wyse, R. F. G. 2003a, *AJ*, 125, 66  
 Conselice, C. J., O’Neil, K., Gallagher, J. S., & Wyse, R. F. G. 2003b, *ApJ*, 591, 167  
 Dalcanton, J. J., Spergel, D. N., Gunn, J. E., Schmidt, M., & Schneider, D. P. 1997, *AJ*, 114, 635  
 Danieli, S., van Dokkum, P., Merritt, A., et al. 2017, *ApJ*, 837, 136  
 Davies, A., Serjeant, S., & Bromley, J. M. 2019, *MNRAS*, 487, 5263  
 De Vicente, J., Sánchez, E., & Sevilla-Noarbe, I. 2016, *MNRAS*, 459, 3078  
 Dey, A., Schlegel, D. J., Lang, D., et al. 2019, *AJ*, 157, 168  
 Di Cintio, A., Brook, C. B., Dutton, A. A., et al. 2017, *MNRAS*, 466, L1  
 Dietterich, T. G. 2000, *Multiple Classifier Systems*, 1  
 Domingos, P. & Hulten, G. 1999, in *Proceedings of the fifth ACM SIGKDD international conference on Knowledge discovery and data mining*, ACM, 155–164

- Dosovitskiy, A., Beyer, L., Kolesnikov, A., et al. 2021, in 9th International Conference on Learning Representations, ICLR 2021, Virtual Event, Austria, May 3-7, 2021 (OpenReview.net)
- Driver, S. P. 1999, *ApJ*, 526, L69
- Du, W., Cheng, C., Zheng, Z., & Wu, H. 2020, *The Astronomical Journal*, 159, 138
- E Greene, J., Greco, J. P., Goulding, A. D., et al. 2022, *ApJ*, 933, 150
- Efron, B. & Gong, G. 1983, *The American Statistician*, 37, 36
- Erwin, P. 2015, *ApJ*, 799, 226
- Ettori, S. & Balestra, I. 2009, *A&A*, 496, 343
- Euclid Collaboration, Scaramella, R., Amiaux, J., et al. 2022, *A&A*, 662, A112
- Fitzpatrick, E. L. 1999, *PASP*, 111, 63
- Flaugher, B., Diehl, H. T., Honscheid, K., et al. 2015, *AJ*, 150, 150
- Fu, J., Liu, J., Tian, H., et al. 2019, in 2019 IEEE/CVF Conference on Computer Vision and Pattern Recognition (CVPR) (Los Alamitos, CA, USA: IEEE Computer Society), 3141–3149
- Galaz, G., Frayer, D. T., Blańa, M., et al. 2022, *ApJ*, 940, L37
- Glorot, X. & Bengio, Y. 2010, in *JMLR Proceedings*, Vol. 9, Proceedings of the Thirteenth International Conference on Artificial Intelligence and Statistics, AISTATS 2010, Chia Laguna Resort, Sardinia, Italy, May 13-15, 2010, ed. Y. W. Teh & D. M. Titterton (JMLR.org), 249–256
- Greco, J. P., Greene, J. E., Strauss, M. A., et al. 2018, *ApJ*, 857, 104
- Haberzettl, L., Bomans, D. J., & Dettmar, R. J. 2007, *A&A*, 471, 787
- Hayward, C. C., Irwin, J. A., & Bregman, J. N. 2005, *ApJ*, 635, 827
- Hewett, P. C. 1982, *MNRAS*, 201, 867
- Huang, K.-W., Chih-Fan Chen, G., Chang, P.-W., et al. 2022, *arXiv e-prints*, arXiv:2210.04143
- Impey, C., Bothun, G., & Malin, D. 1988, *ApJ*, 330, 634
- Ivezić, Ž., Kahn, S. M., Tyson, J. A., et al. 2019, *ApJ*, 873, 111
- Jarvis, M. 2015, *TreeCorr*: Two-point correlation functions, *Astrophysics Source Code Library*, record ascl:1508.007
- Jia, P., Sun, R., Li, N., et al. 2023, *AJ*, 165, 26
- Junais, Boissier, S., Boselli, A., et al. 2022, *A&A*, 667, A76
- Junais, Boissier, S., Epinat, B., et al. 2020, *A&A*, 637, A21
- Kingma, D. P. & Ba, J. 2015, in 3rd International Conference on Learning Representations, ICLR 2015, San Diego, CA, USA, May 7-9, 2015, Conference Track Proceedings, ed. Y. Bengio & Y. LeCun
- Kobayashi, Y., Nishimichi, T., Takada, M., & Miyatake, H. 2022, *Phys. Rev. D*, 105, 083517
- Koda, J., Yagi, M., Yamanoi, H., & Komiyama, Y. 2015, *ApJ*, 807, L2
- Koo, D. C. & Szalay, A. S. 1984, *ApJ*, 282, 390
- La Marca, A., Iodice, E., Cantiello, M., et al. 2022a, *A&A*, 665, A105
- La Marca, A., Iodice, E., Cantiello, M., et al. 2022b, *A&A*, 665, A105
- Landy, S. D. & Szalay, A. S. 1993, *ApJ*, 412, 64
- Laudato, E. & Salzano, V. 2023, *European Physical Journal C*, 83, 402
- Leisman, L., Haynes, M. P., Janowiecki, S., et al. 2017, *ApJ*, 842, 133
- Lim, S., Côté, P., Peng, E. W., et al. 2020, *ApJ*, 899, 69
- Liutkus, A., Cifka, O., Wu, S., et al. 2021, in *Proceedings of Machine Learning Research*, Vol. 139, Proceedings of the 38th International Conference on Machine Learning, ICML 2021, 18-24 July 2021, Virtual Event, ed. M. Meila & T. Zhang (PMLR), 7067–7079
- Ma, C.-P. & Fry, J. N. 2000, *ApJ*, 543, 503
- Mancera Piña, P. E., Aguerrí, J. A. L., Peletier, R. F., et al. 2019, *MNRAS*, 485, 1036
- Mancera Piña, P. E., Peletier, R. F., Aguerrí, J. A. L., et al. 2018, *MNRAS*, 481, 4381
- Marleau, F. R., Habas, R., Poulain, M., et al. 2021, *A&A*, 654, A105
- Martin, G., Kaviraj, S., Laigle, C., et al. 2019, *MNRAS*, 485, 796
- McConnachie, A. W. 2012, *AJ*, 144, 4
- McGaugh, S. S. 1996, *MNRAS*, 280, 337
- McGaugh, S. S. & Bothun, G. D. 1994, *AJ*, 107, 530
- Mihos, J. C., Durrell, P. R., Ferrarese, L., et al. 2015, *ApJ*, 809, L21
- Mihos, J. C., Harding, P., Feldmeier, J. J., et al. 2017, *ApJ*, 834, 16
- Minchin, R. F., Disney, M. J., Parker, Q. A., et al. 2004, *MNRAS*, 355, 1303
- Mo, H. J., McGaugh, S. S., & Bothun, G. D. 1994, *MNRAS*, 267, 129
- Morganson, E., Gruendl, R. A., Menanteau, F., et al. 2018, *PASP*, 130, 074501
- Neilsen, E. J., Annis, J. T., et al. 2019, *Dark Energy Survey's Observation Strategy, Tactics, and Exposure Scheduler*, Tech. rep.
- Neuschaefer, L. W., Windhorst, R. A., & Dressler, A. 1991, *ApJ*, 382, 32
- O'Neil, K. & Bothun, G. 2000, *ApJ*, 529, 811
- Parmar, N., Ramachandran, P., Vaswani, A., et al. 2019, in *Advances in Neural Information Processing Systems 32: Annual Conference on Neural Information Processing Systems 2019, NeurIPS 2019, December 8-14, 2019*, Vancouver, BC, Canada, 68–80
- Peacock, J. A. & Smith, R. E. 2000, *MNRAS*, 318, 1144
- Pearson, W. J., Suelves, L. E., Ho, S. C. C., et al. 2022, *A&A*, 661, A52
- Peebles, P. J. E. 1980, *The large-scale structure of the universe*
- Peebles, P. J. E. & Hauser, M. G. 1974, *ApJS*, 28, 19
- Peng, C. Y., Ho, L. C., Impey, C. D., & Rix, H.-W. 2002, *AJ*, 124, 266
- Pérez-Carrasco, M., Cabrera-Vives, G., Martínez-Marin, M., et al. 2019, *PASP*, 131, 108002
- Pimentel, Ó., Estévez, P. A., & Förster, F. 2023, *AJ*, 165, 18
- Poulain, M., Marleau, F. R., Habas, R., et al. 2021, *MNRAS*, 506, 5494
- Prole, D. J., van der Burg, R. F. J., Hilker, M., & Davies, J. I. 2019, *MNRAS*, 488, 2143
- Prole, D. J., van der Burg, R. F. J., Hilker, M., & Spitler, L. R. 2021, *MNRAS*, 500, 2049
- Robitaille, T. & Bressert, E. 2012, *APLpy: Astronomical Plotting Library in Python*, *Astrophysics Source Code Library*, record ascl:1208.017
- Rojas, K., Savary, E., Clément, B., et al. 2022, *A&A*, 668, A73
- Román, J. & Trujillo, I. 2017, *MNRAS*, 468, 4039
- Russakovsky, O., Deng, J., Su, H., et al. 2015, *Int. J. Comput. Vis.*, 115, 211
- Saburova, A. S., Chilingarian, I. V., Kasparova, A. V., et al. 2021, *MNRAS*, 503, 830
- Saburova, A. S., Chilingarian, I. V., Kulier, A., et al. 2023, *MNRAS*, 520, L85
- Sandage, A. & Binggeli, B. 1984, *AJ*, 89, 919
- Schaefer, C., Geiger, M., Kuntzer, T., & Kneib, J.-P. 2018, *A&A*, 611, A2
- Schlafly, E. F. & Finkbeiner, D. P. 2011, *ApJ*, 737, 103
- Schlegel, D. J., Finkbeiner, D. P., & Davis, M. 1998, *ApJ*, 500, 525
- Sevilla-Noarbe, I., Bechtol, K., Carrasco Kind, M., et al. 2021, *ApJS*, 254, 24
- Simon, J. D. 2019, *ARA&A*, 57, 375
- Simonyan, K. & Zisserman, A. 2015, in 3rd International Conference on Learning Representations, ICLR 2015, San Diego, CA, USA, May 7-9, 2015, Conference Track Proceedings, ed. Y. Bengio & Y. LeCun
- Sprayberry, D., Impey, C. D., Bothun, G. D., & Irwin, M. J. 1995, *AJ*, 109, 558
- Strateva, I., Ivezić, Ž., Knapp, G. R., et al. 2001, *AJ*, 122, 1861
- Su, J., Lu, Y., Pan, S., Wen, B., & Liu, Y. 2021, *CoRR*, abs/2104.09864 [2104.09864]
- Tan, A., Nguyen, D. T., Dax, M., Nießner, M., & Brox, T. 2021, in *Thirty-Fifth AAAI Conference on Artificial Intelligence, AAAI 2021, Thirty-Third Conference on Innovative Applications of Artificial Intelligence, IAAI 2021, The Eleventh Symposium on Educational Advances in Artificial Intelligence, EAAI 2021, Virtual Event, February 2-9, 2021*, 9799–9807
- Tanoglidis, D., Čiprijanović, A., & Drlica-Wagner, A. 2021a, *Astronomy and Computing*, 35, 100469
- Tanoglidis, D., Drlica-Wagner, A., Wei, K., et al. 2021b, *ApJS*, 252, 18
- Thuruthipilly, H., Grespan, M., & Zdrożny, A. 2022a, *arXiv e-prints*, arXiv:2212.12915
- Thuruthipilly, H., Zdrożny, A., Pollo, A., & Biesiada, M. 2022b, *A&A*, 664, A4
- van der Burg, R. F. J., Muzzin, A., & Hoekstra, H. 2016, *A&A*, 590, A20
- van Dokkum, P. G., Abraham, R., Merritt, A., et al. 2015, *ApJ*, 798, L45
- Vaswani, A., Shazeer, N., Parmar, N., et al. 2017, in *Advances in Neural Information Processing Systems 30: Annual Conference on Neural Information Processing Systems 2017, December 4-9, 2017*, Long Beach, CA, USA, 5998–6008
- Venhola, A., Peletier, R., Laurikainen, E., et al. 2019, *A&A*, 625, A143
- Wang, X., Kondratyuk, D., Christiansen, E., et al. 2022, in *International Conference on Learning Representations*
- Wittmann, C., Lisker, T., Ambachew Tilahun, L., et al. 2017, *MNRAS*, 470, 1512
- Wortsman, M., Ilharco, G., Gadre, S. Y., et al. 2022, in *ICML*, 23965–23998
- Xu, W., Ramos-Ceja, M. E., Pacaud, F., Reiprich, T. H., & Erben, T. 2022, *A&A*, 658, A59
- Yasuda, N., Fukugita, M., Narayanan, V. K., et al. 2001, *AJ*, 122, 1104
- Yu, J., Wang, Z., Vasudevan, V., et al. 2022, *Trans. Mach. Learn. Res.*, 2022
- Zehavi, I., Zheng, Z., Weinberg, D. H., et al. 2005, *ApJ*, 630, 1
- Zhang, H., Goodfellow, I. J., Metaxas, D. N., & Odena, A. 2018, *CoRR*, abs/1805.08318 [1805.08318]
- Zhao, H., Jia, J., & Koltun, V. 2020, *CoRR*, abs/2004.13621 [2004.13621]
- Zheng, Z., Berlind, A. A., Weinberg, D. H., et al. 2005, *ApJ*, 633, 791